Pore-Scale Visualization of CH_4 Gas Hydrate Dissociation under Permafrost Conditions

Pandey, Jyoti Shanker; Almenningen, Stian; von Solms, Nicolas; Ersland, Geir

Published in:
Energy & Fuels

Link to article, DOI:
10.1021/acs.energyfuels.0c03295

Publication date:
2021

Document Version
Peer reviewed version

Pore-Scale Visualization of CH_4 Gas Hydrate Dissociation under Permafrost Temperature Conditions

Jyoti Shanker Pandey[1]', Stian Almenningen[2], Nicolas von Solms[1] and Geir Ersland[2,*]*

1 Center for Energy Resource Engineering (CERE), Department of Chemical and Biochemical Engineering, Technical University of Denmark, 2800 Kgs. Lyngby, Denmark

2 Department of Physics, University of Bergen, Norway

KEY WORDS: CH_4 gas hydrate dissociation, Permafrost, High-Pressure Micromodels.

ABSTRACT

In this study, we demonstrate the effectiveness of combined production technique involving depressurization and thermal stimulation for gas production from CH_4 gas hydrates in subzero temperature range between -3°C to 0°C. CH_4 gas hydrate phase transitions during formation, depressurization, re-formation, self –preservation, thermal stimulation stage were visualized using a high-pressure, water-wet, silicon-wafer micromodel with pore network of actual sandstone rock. A set of eight experiments were performed in which CH_4 gas hydrate was formed at a constant pressure between 60 – 85 bar and constant temperature between 0 °C – 4°C. CH_4 gas hydrate was

then dissociated at constant system temperature between -3 °C to - 2 °C by pressure depletion to study the effect of hydrate and fluid saturation on dissociation rate, self-preservation, and risk of ice formation. The dissociation rate and behaviour were heavily affected by the total hydrate saturation and initial hydrate distribution in the pore space. Additionally, the amount of produced CH_4 gas was limited below 0 °C due to the rapid formation of ice from the liquid water that was liberated from the initial hydrate dissociation. The liberated CH_4 gas was therefore immobilized and trapped by the formed ice and could not be produced without thermal stimulation. Thermal stimulation removed the blockage of pore space caused by ice and secondary hydrate formation and enhanced gas production. Visual observation showed self-preserved hydrates in metastable state dissociated before ice below subzero temperature providing experimental evidence of recently discovered methane leaking from gas hydrate deposits due to global warming. The results highlight the influence of heterogeneity in hydrate distribution and total saturation on the hydrate dissociation behaviour below 0 ℃ temperature. Micromodel observation provides direct insights into hydrate dissociation, self-preservation, fluid migration, gas coalescence, ice and secondary hydrate formation at pore scale below subzero temperature.

1. Introduction

Experimental modelling of methane (CH_4) gas hydrate formation, dissociation, and phase stability in permafrost sediments are essentially related to global warming and in schemes for CH_4 recovery and/or carbon dioxide (CO_2) storage. CH_4 gas hydrate is an ice-like crystalline substance formed by CH_4 gas and water at moderate-to-high pressure and low-temperature conditions [1]. CH_4 gas hydrate in sediments is of particular interest due to the vast amount of gas hydrate reserves discovered in shallow permafrost sediments and on continental margins in the marine environment

[2]. These deposits may provide large volumes of Natural Gas in the future; therefore, gas production via dissociation of sedimentary CH_4 gas hydrate is a topic of intense research. Hydrate dissociation via depressurization is a well-studied phenomenon both at lab-scale as well as through field trials and is considered as the most cost-effective and well-understood production technique to be implemented at commercial scale [3]. Still, there are challenges associated with hydrate dissociation such as changes in physical properties [4], risk of hydrate re-formation, sand and water production, and discontinued gas production [5].

Permafrost environment, including ice containing frozen soil, rock or sediments at or below 0°C provides favorable thermodynamic conditions for gas hydrate occurrence. A hydrate stability zone within permafrost and below permafrost and its thickness is controlled by permafrost layer temperature, the geothermal gradient of sediments in permafrost and below the permafrost, pore fluid salinity, gas chemistry, gas and water saturation, formation pore pressure and the difference between pore pressure and hydrostatic pressure [6]. Permafrost temperature varies according to longitude/latitude and altitude. For example, it is reported that the annual average geothermal temperature in the permafrost layer in Qinghai- Tibet plateau is between -4°C to 0°C [7]. Permafrost based hydrate deposits are characteristically different from oceanic hydrates due to relatively low concentration of salts in permafrost lead to lower and delayed gas production from permafrost, shallow depth cause lower sensible heat of reservoir thus controlling rate of fluid withdrawal and a higher level of hydrate saturation presence in permafrost [8]. It is reported that gas hydrates in permafrost sediments are usually located at 200-250 m within the permafrost zone and/or 800-1500 m below the permafrost regions [9]. Hydrates within frozen rocks found in the Bovanekovo Gas Field in West Siberia permafrost have an ice saturation (25%-85%) and unfrozen water saturation (2%-20%), varying with depth [10]. Unfrozen pore water is defined as the amount of pore

liquid water in equilibrium with gas hydrate and ice at elevated pressure at a subzero temperature in sediments. Hydrate deposits have also been found in shallow depths of 50-70 m in the Mackenzie Delta, Canada, suggesting the presence of preserved pore hydrate outside the thermodynamic stability zone [9]. These metastable hydrates have very low dissociation rates due to the self-preservation behaviour associated with subzero temperatures. Here, gas hydrates and ice coexist, and the gas hydrates are covered with thin ice sheets that delay hydrate dissociation [11–17].

Several theories have been proposed to explain the self-preservation effect. Zhong et al. [18] studied the self-preservation effect on the dissociation of CH_4 gas hydrate below 0 °C using Raman spectroscopy and confirmed the role of the guest molecule on hydrate self-preservation nature. Takeya et al. [19] proposed it to be due to the interaction between guest and water molecules. According to Giavarini et al. [20], high hydrate saturation shows weaker self-preservation effect due to less entrapped water or ice. The decrease in temperature below 0 °C, would improve self-preservation and reduce dissociation rate. Studies also show that below subzero temperatures, pressure increase improves self-preservation [14,21,22] due to collapse of pore space by sintered ice [23] and an increase in dissociation temperature [24]. During the pressurization, unfrozen residual pore water present in frozen sediments could convert into pore ice and enhance self-preservation during dissociation due to subsequent annealing of the surrounded ice coating [25,26].

Two-dimensional micromodels offer a unique opportunity to perform pore-scale visualization during the formation and dissociation of hydrate at high resolution using artificial sedimentary rock [27]. Current micromodels are fabricated to work in the high-pressure environment, equipped with actual geological, topographical properties and pore-scale geometry of real rocks. Micromodels offer a non-destructive, low-cost solution and shorter experiments compared to other pore-scale techniques, such as x-ray computer tomography (CT) scanning and magnetic resonance

85 imaging. The micromodels have previously been used to visualize hydrate formation in the
86 presence of water-soluble tetrahydrofuran (THF) at atmospheric pressure and with CH_4/CO_2
87 saturated water at high pressure [28]. Direct visualization showed hydrate formation from the vapor
88 saturated liquid phase, the formation of hydrate in the centre of pore space in water wet
89 micromodels, isolated gas bubble conversion into hydrates, and redistribution of gas hydrate with
90 time. Katsuki et al. [29] used a glass micromodel to study the subcooling effect on hydrate growth
91 kinetics. Direct visualization showed the conversion of dendritic hydrate into particulate hydrate
92 system at higher subcooling temperature (greater than 12 K). Hauge et al. [30] discussed the
93 formation of CH_4 and CO_2 hydrate using high-pressure silicon micromodels and concluded that
94 growth pattern is dependent on fluid connectivity and local fluid distribution. Almenningen et al.
95 [31] discussed the experimental protocol to calculate the thermodynamics of hydrate formation and
96 dissociation using high-pressure micromodel. Almenningen et al. also studied the salinity effect
97 on hydrate dissociation [32] and CO_2 hydrate formation in the porous medium [33] using high-pressure
98 micromodels. So far, the dissociation behaviour of CH_4 gas hydrate using micromodels [31,32] is
99 studied above 0°C. CH_4 gas hydrate dissociation is dependent on initial hydrate saturation, hydrate
100 morphology, and the mobility of the fluid phases; however, hydrate dissociation below subzero
101 temperature is not well understood. Thus, a fundamental understanding of CH_4 gas hydrate
102 distribution, dissociation mechanism, and self-preservation in sediments at the pore-scale level are
103 essential to optimize the CH_4 gas production method from permafrost-affected hydrate reservoirs.
104 Recent work has focused on hydrate formation in frozen rocks and ice-to-hydrate conversion in
105 free space or pore space, but few studies have been subject to dissociation and self-preservation of
106 hydrate in pore space in permafrost [9].

This study provides a quantitative analysis of CH_4 gas hydrate dissociation below 0 °C using a high-pressure micromodel network replicating a cross-section of porous sandstone rock. Direct optical visualization of dissociation behaviour at pore-scale provides a fundamental understanding of the effect of various parameters, including temperature, hydrate saturation, and free gas in the pore space on the dissociation behaviour in coarse-grained sediments. Optical access to pore-scale visualization offers identification of different mechanisms activated below 0°C, including self-preservation, hydrate re-formation, and gas trapping.

2. Materials and Methods

2.1 Experimental Setup

The micromodel setup (Figure 1) included four key elements. The micro model, visualization assembly, the high-pressure/low-flow rate pumps, and the cooling system. Micromodel assembly includes high-pressure micromodel with stand placed inside dual-chamber filled with water/glycol. A dual-chamber design facilitates temperature control and pore space visualization. The micromodel was made of a silicon wafer that was anodically bonded to a borosilicate glass wafer. The rectangular micromodel was 2.8 cm long and 2.2 cm wide. The realistic two-dimensional pore network of Berea sandstone was etched into the silicon wafer with the deep reactive ionic etching (DRIE) technique that developed a two-dimensional vertical profile with constant height throughout the cross-section. Anodic bonding was performed to isolate the flow path under a high-pressure environment to facilitate direct visual observation. Due to the high aspect ratio and large coordination number, the model carried realistic capillary forces of similar scale found in actual rock [31]. The micromodel was water wet in nature, and wettability was uniform. The solid grains were thus coated with thin water films, and the pores were filled with

water, gas or hydrate. The water-wet nature of solid grains induced a curved interface between liquid and gas and allowed for visual differentiation between fluid phases. The model consisted of average pore diameter of 100 µm and a constant vertical height of 25 µm.

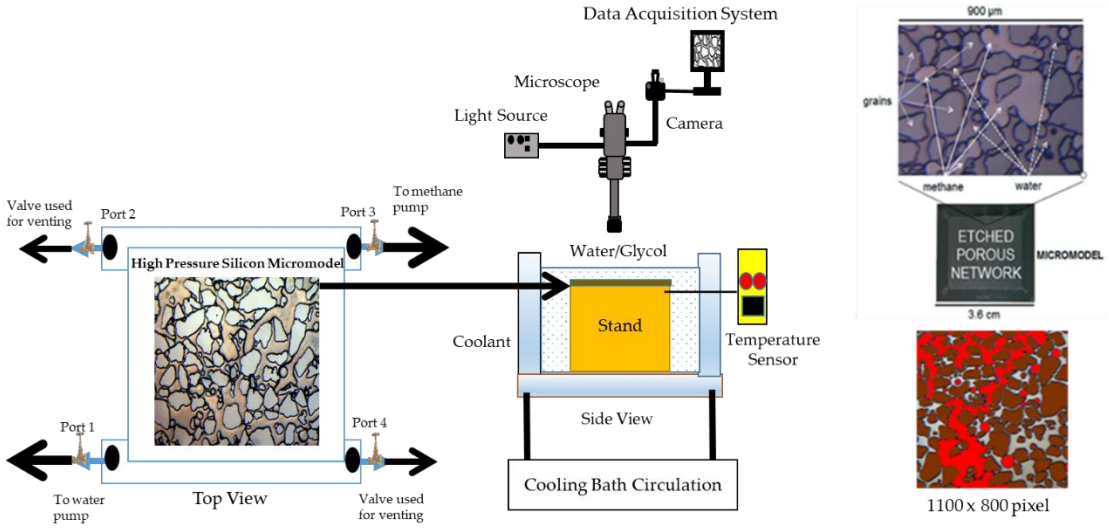

Figure 1 A layout of the experimental setup (subfigure A and B) and field of view (FOV) cross-section of the micromodel (Sub figure C). For better visualization, images are segmented, and phases are highlighted in different colours. The solid grain is shown in brown, gas in red and water in blue. Spatial scale of the images used in this study is 1100 x 800 pixel.

The micromodel had four nano ports with nano-tubing guiders and rubber packing (Upchurch/IDEX), connected to high-pressure pumps using a combination of 1/16" PEEK tubing and 1/8" steel tubing. Ports were used for injection/production of liquid/gas. It was placed between two steel casings to ensure it remained still during the experiment. The micromodel was carefully placed on the stand and lowered into the inner cooling chamber. Due to steel-casing, the micromodel was able to withstand pressures up to 150 bar. A high-pressure (HP) pump controls the pore pressure, and flow of water (port 1) and CH4 (port 3) situated diagonal opposite. CH_4 pressure inside the micromodel was controlled by a dual-piston high-pressure pump (Chandler Engineering, Quizix Q5200). FOV of pore space inside micromodel generated as a Top view from

Stereomicroscope. FOV is partially saturated with gaseous CH4 and liquid water. The gaseous phase and liquid phase are differentiate based on the contrast difference between the liquid and gas phase. Gas-phase being brighter than the liquid phase and separated by a sharp interface and a curvature towards the hydrophilic grains. Images are segmented to enhance the visualization. Gas-phase is represented in red colour while grains are coloured as brown. Later, the water phase is represented in blue colours. Valves at port 2 and port 4 were used for venting. The micromodel was placed on the holder, fully submerged into glycol in the inner chamber of the custom-designed, dual-chamber water bath. Glycol was used to achieve a temperature below 0°C without freezing. The outer chamber was insulated to reduce heat loss and to have better temperature control. The outer chamber and inner chamber were separated by aluminium walls, which allowed rapid heat exchange between the inner and outer chamber. Cooling fluid (water mixed with antifreeze) was circulated between the inner and outer chamber using the cooling bath to achieve the desired temperature. The temperature was measured by a thermocouple (HH506RA Omega Multi-logger, Type K), placed directly beneath the micromodel. The dual-chamber was placed above the anti-vibration platform. A stereomicroscope (Nikon SMZ1500) with DSLR camera (NikonD7100) was used for visualization and recording. The working distance was 54 mm, and field of view (FOV) was of the order of 2 mm using 1X objective lenses and 110X magnification. A light source (Photonic LED F1, cold light 5500K) was installed to record clear images, and the camera was connected to a monitor for improved image interpretation.

Phase saturation was calculated using the image processing software Paint.net. Different phases were segmented whenever it was necessary, and two-dimensional fluid saturation was estimated using the pixel count method. In this method, each colour cover specific image area expressed in

the number of pixels. The two-dimensional fluid saturation for the phase "i" (S_i) were estimated using the following formula.

$$S_i = \frac{A_i}{A_v} = \frac{N_i}{N_v} = \frac{N_i}{N_{tot} - N_{grains}} \quad (1)$$

Where A_i is the area of the phase (Gas, water or hydrate) in the given image after segmentation. N_i is the number of pixels for phase (gas, liquid or water). N_v, N_{tot}, N_{grains} are the number of void pixels, total number of pixels in the image and number of pixels corresponding to grains respectively. Both porous hydrates (grey colour) and non-porous hydrates (transparent-crystalline) were considered to calculate two-dimensional hydrate saturation. This method has a few limitations. Phase saturation was obtained locally (approx. 1% of the total micromodel area) within FOV, which could be different from saturation in the entire micromodel. The phase saturation calculation was based on the assumption that pore space was saturated with single fluid; however, it may be possible that based on hydrate morphology, multiple phases coexisted within the pore depth of 25 μm.

2.2 Experimental procedure and data processing

The micromodel was flushed with water to remove residual air, followed by distilled water injection into the pore space via port 1 (Figure 1). The entire pore space of the micromodel was thoroughly studied to ensure 100% water saturation. The water pore pressure was increased to 60 bar by injection water while keeping the remaining ports closed. The methane pump pressure was increased to 61 bar and subsequently, a valve at port 3, was opened to make a connection between CH_4 gas and water inside micromodel. After that, the water pore pressure was reduced to 59 bar to allow CH_4 gas to enter into micromodel and appear in FOV. Thereafter, the valve at port 1 was

188 closed, and the methane pump was kept at a constant pressure operating mode. The methane pump
189 pressure kept constant for 24 hours to allow CH_4 gas to dissolve into the water and to check the
190 high-pressure system for leaks. Once the water was thoroughly saturated with methane, the
191 temperature was brought down within the hydrate formation zone to trigger hydrate formation.
192 During the cooling down, additional gas dissolved in the water due to the increase in gas solubility
193 at a lower temperature, and some of the gas bubbles within the FOV disappeared. In those case,
194 when hydrate formation was not triggered within a couple of hours after the temperature had
195 stabilized, the sudden and temporary turbulence was created within the pore space by venting gas
196 through port 4 by quick opening/closing of the valve [32]. After the system returned to static
197 conditions (constant pressure, no flow), hydrate nucleation usually followed within minutes.
198 Pressure differential (Difference in pressure between micromodel and atmospheric pressure due to
199 port opening) developed during agitation, caused dissolved gas liberation from water, and gas-
200 water contact was surface-enhanced, and nucleation was initiated. The growth pattern was then
201 monitored and recorded until there were no further phase changes occurring (usually 24 hours).
202 The temperature was reduced below 0°C in the interval between -3°C to -0.1°C to achieve
203 permafrost temperature conditions. To prepare for hydrate dissociation, the valve at port 1 was
204 reopened to establish a connection between the water pump and micromodel. Afterwards, CH_4
205 pump was retracted via port 3 at a constant rate of 30-60 ml/hour until the pressure reached CH_4
206 gas hydrate equilibrium pressure (P_{eq}) at the given temperature (P_{eq}=32 bar for CH_4 gas hydrate at
207 1.5 °C using CSMGem). From P_{eq} and below, the pump was retracted at 10 ml/hour to observe
208 dissociation. During retraction, the water pump pressure was reduced gradually to 35 bar to
209 maintain a manageable pressure difference between the water pump (port 1) and gas pump (port
210 3). Subsequently, the water pump was shut down, but the valve (port 1) remained open to allow

recording of differential pressure during dissociation. The retraction was continued until full dissociation was observed except for some experiments where hydrates did not dissociate even at atmospheric pressure. Thermal stimulation was then needed to finalize hydrate dissociation.

Temperature variation during the experiment would affect dissociation pressure. The uncertainty associated with a thermometer is in the range ±0.1℃ and temperature had the uncertainty of ±0.2℃. The methane gas volume injected/retracted from the pump is an important parameter for calculating hydrate saturation. The fluctuation in room temperature may cause a change in gas volume in the range of ±0.7 ml at 83 bar under ideal gas law.

Table 1 summarizes the P-T conditions and dissociation techniques used for each experiment. The experiments were divided into three different groups based on the dissociation temperature that was used. For experiments 1-3, the dissociation temperature was above 0°C. For experiments 4 and 5, the dissociation temperature was close to 0°C. For experiment 6-8, the dissociation temperature was below 0°C**.** If depressurization (DP) was insufficient to complete hydrate dissociation within 24 hours, thermal stimulation (TS) was additionally used.

Table 1 *Experimental summary of P, T conditions during hydrate formation and dissociation. DP = Depressurization, TS = Thermal stimulation.*

Exp.	Hydrate formation			Hydrate dissociation		
	P (bars)	T (°C)	Method	P_{eq} (bars	T (°C)	Method
1	85	0.9	Agitation	28.4	0.9	DP
2	80	0.8	Agitation	28.1	0.8	DP
3	60	1.0	Memory	28.7	1.0	DP
4	79	1.4	Agitation	25.0	-0.5	DP
5	71	1.5	Agitation	25.4	-0.1	DP+TS
6	80	1.7	Agitation	23.3	-3.0	DP+TS
7	55	1.9	Memory	23.4	-2.6	DP
8	80	2.0	Agitation	23.4	-2.7	DP+TS

For all experiments excluding 3 and 7, agitation was used to initiate hydrate nucleation effectively. During experiments 3 and 7, hydrate nucleation occurred quickly without any agitation due to the memory effect of water, which had pressure and temperature history from previous experiments.

3. Results and Discussion

Micromodel experiments were carried out to visualize the dissociation behaviour at different dissociation temperatures both below and above 0 °C to discuss the methane hydrate phase change during depressurization, self-preservation and re-formation stage. The qualitative study was performed to study the gas production behaviour from methane hydrate reservoir under different hydrate saturation and arrangement within pore space under subzero temperature conditions.

3.1. Hydrate formation at constant P and T > 0°C

Direct visualization confirmed that hydrate nucleation and subsequent growth is a rapid process described as a heterogeneous front movement along with fluid interfaces. The hydrate formation started at the gas and water interface [28,29,34] and encapsulated the gas phase by hydrate films (HF). Initial water and gas saturation and mass transfer of gas/water molecules across the hydrate film controlled the hydrate film vertical thickness [35]. The thickness of the hydrate film between the gas-liquid interface has previously been estimated to be 10-20μm [27,36,37]. The gas bubbles were usually fully consumed in areas with low gas saturation, whereas gas remained coated by hydrate films in areas with high gas saturation and limited availability of water [23]. Hydrate formation in the water phase was also observed when liquid water was saturated with dissolved methane [29,38]. Crystallization of hydrates in the water phase led to transparent hydrate crystals (HC) that were easily distinguishable from the dark-grey coloured hydrate films because of the difference in refractive indexes between gas, water, and hydrates (Gas hydrate = 1.35, Water =1.33, gas = 1) [39].

Laboratory studies deal with the oversupply of gas, whereas in nature, hydrate formation is controlled by limited gas supply that leads to crystalline hydrates as pore water is over-saturated with gas. Table 2 provides the information regarding hydrate formation pressure, temperature, subcooling temperature, observed hydrate morphology and change in different phase saturations before and after hydrate formation and hydrate distribution. The fluid saturations were quantified based on image analysis and provide an estimation of the 2D fluid saturations.

Table 2 Experimental summary of P, T conditions and fluid saturations during hydrate formation. HF = Hydrate films, HC= Hydrate crystals, Teq-T = Subcooling. Teq was calculated using CSMGem, HM = Hydrate morphology

	Constant P, T			**Before formation**		**After formation**			
Exp.	P(bars)	T(°C)	T_{eq}-T	S_{iw}	S_{ig}	S_W	S_g	S_H	HM
1	85	0.9	10.6	10 %	90 %	1 %	6 %	93 %	HF
2	76	0.8	9.7	93 %	7 %	92 %	0 %	8 %	HC
3	60	1.0	7.2	61 %	39 %	8%	4%	88 %	HF, HC
4	79	1.4	9.4	57 %	43 %	1 %	5 %	95 %	HF
5	71	1.5	8.3	56 %	44 %	16 %	0 %	84 %	HC
6	80	1.7	9.2	50 %	50 %	7 %	2 %	91 %	HF, HC
7	55	1.9	5.5	53 %	47 %	12 %	1 %	87 %	HF
8	80	2.0	8.9	87 %	13 %	74 %	1 %	25 %	HF, HC

In general, hydrate morphology in pore space could be grain cementing or pore-filling. For S_{iw} = 0.35, or above, hydrate formed are pore filling [40,41]. Ohmura et al. [42] studied the methane hydrate morphology experimentally and found that system pressure does not influence the formation mechanism. Methane hydrate formed at gas-liquid interface and later hydrate grew into liquid water due to methane solubility. Many morphology-based studies suggest that hydrate crystals morphology depends on the applied driving force. Several morphologies studies suggest that Hydrate crystals morphology depends on applied driving force such that at higher driving force, crystal growth would become more random due to faster nucleation at different locations [43].

Figure 2 summarizes the hydrate morphologies observed after hydrate formation at constant T above 0°C. The field of view includes porous HF, non-porous HC, pore water, and gaseous CH_4. Figure Exp.3a, 5.a and 7.a show initial gas and liquid saturation and distribution before hydrate formation starts. The difference in initial conditions leads to heterogeneity defined by the difference in hydrate saturation and distribution, as shown in Figure Exp.3c, 5.c and 7.c. It is common practice to modelled hydrate systems as homogenous systems and constant hydrate saturation at pore scale during the gas production modelling [4445] however natural hydrate system is complex, and hydrate distribution is heterogeneous [46]. Heterogeneity would cause the development of a preferential pathway for fluid migration during the depressurization.

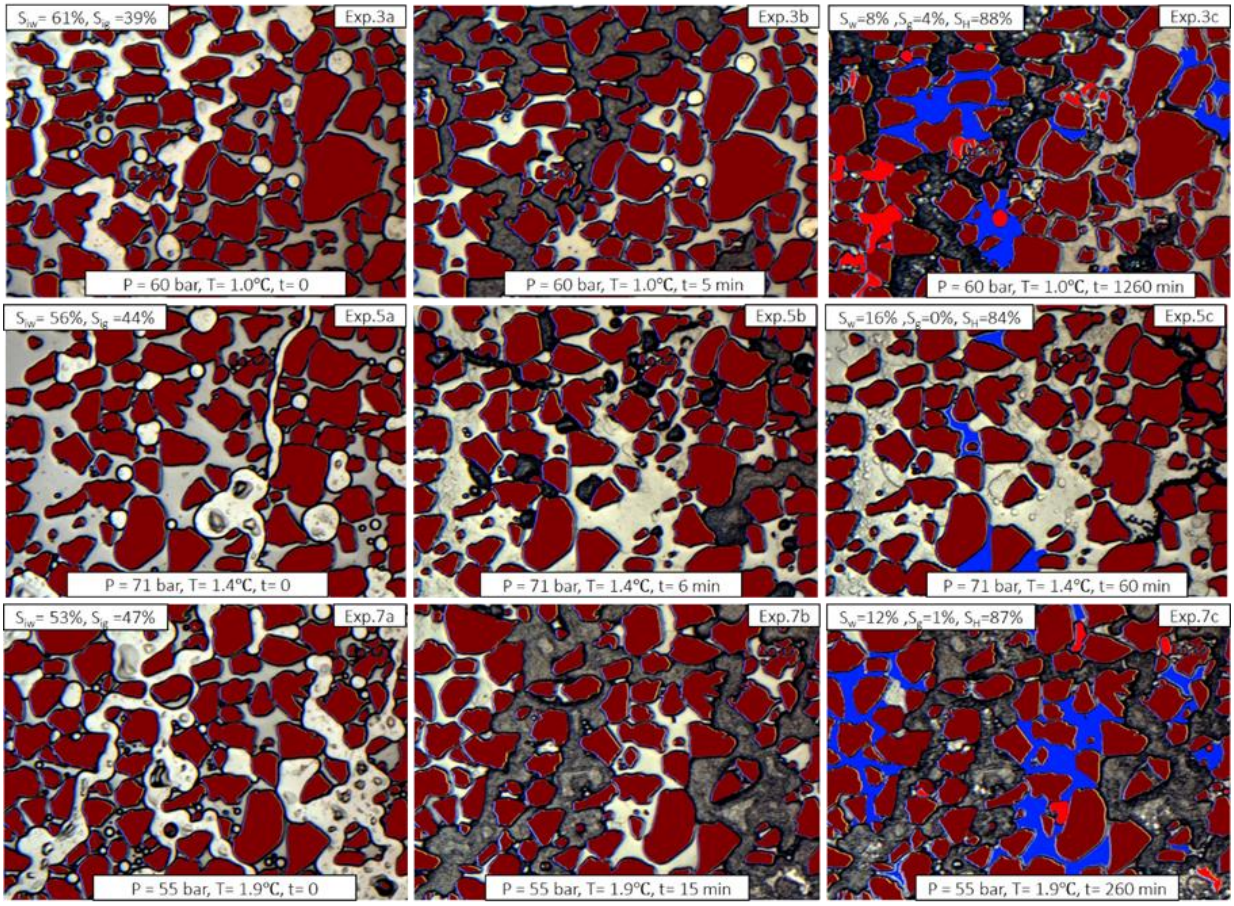

Figure 2. *Overview of three different hydrate distribution patterns (Exp. 3, 5, and 7) in the pore space at T> 0°C. The silicon grains, liquid water, and gaseous CH_4 are coloured brown, blue, and red, respectively when required. The CH_4 gas hydrate phase*

is not segmented, and porous hydrate films (HF) are observed in dark grey and non-porous crystalline hydrate (HC) in transparent white. Figure Exp.3c, Exp.5c and Exp.7c show three different hydrate morphology at the end of the formation. Field of view in Figure Exp.3a shows equal water and methane gas saturation. During hydrate formation, gas dissolved into water and hydrate film encapsulating the gas phase as shown in figure Exp.3b. Figure Exp.3c displays both porous and non-porous hydrates along with unconsumed liquid water and CH_4 gas. Shows hydrate morphology distribution, including hydrate crystals and hydrate film. Field of view in figure Exp.5a shows high S_{iw} and low S_{ig} before the start of hydrate formation. During hydrate formation, methane gas saturated water crystalized first, as shown in figure Exp.5b. Field of view after 60 minutes in figure Exp.5c displays non-porous and liquid water. All gas consumed during hydrate growth. Figure Exp.7a illustrates high S_{ig} and low S_{iw}. Figure Exp.7b displays HF encapsulating CH_4 Gas in the middle of the pores as well as some HC. Figure Exp.7c displays both porous hydrates and unconsumed liquid water and CH_4 gas.

The figure 2 above confirms that hydrate distribution within pore space is characterized as heterogeneous due to different initial conditions, including pressure and temperature, initial fluid saturations and distribution. Pore-scale heterogeneity in hydrate saturation would create uncertainty in gas production behaviour, and production rate can vary up to ± 25% [47]. Lab-scale experiments using different formation techniques also confirm heterogeneous methane hydrate formation in pore space [48].

Experiment 1 started with high gas saturation, S_{ig}=90%, and HF formed and encapsulated the gas phase. Experiment 2 had high initial water saturation, S_{iw} = 93%, and HC were formed, and the gas was fully consumed. Experiment 3 has initial water and gas saturation equal to 61% and 39% respectively, and hydrate distribution included HC and HF. Subcooling temperature (T_{eq}-T) varied between 5.5 to 10.6 ℃ however, no correlation between subcooling and hydrate morphology was observed. Additionally, the growth pattern during hydrate formation also depends on pore size distribution, pore throats, and capillary forces that control initial water and gas distribution.

3.2. Phase transitions during cooling to T < 0 °C at constant P

The change in water, gas and hydrate saturations were recorded and quantified during cooling of the micromodel from T > 0°C to T < 0°C at constant pressure (Table 3). However, the similar texture and refractive index between CH_4 hydrates and ice made it difficult to distinguish the two phases from one another. Thin layers of ice formed close to the grain surface could neither be identified due to limitations of the magnification power. Additionally, metastable unfrozen pore water was always present after cooling to subzero temperature [49]. Some of the pore water in permafrost does not convert into ice because of the freezing temperature of the water is depressed below 0℃ due to confining pressure, dissolved salts and capillary forces.

Table 3 *Change in fluid saturation during cooling below 0 °C. HF = Hydrate films, HC= Hydrate Crystals,(Tf= Formation Temperature above 0 ℃, Tf1=formation temperature below 0 ℃) Sfw = Final water saturation below 0℃, Sfg = final gas saturation below 0℃. HM = Hydrate Morphology*

	Cooling		**Above 0°C**			**Below 0°C**			
Exp	**T_f (°C)**	**T_{fl}(°C)**	**S_{iw}**	**S_{ig}**	**S_H**	**S_{fw}**	**S_{fg}**	**S_H/S_{ice}**	**HM**
4	1.4	-0.5	1 %	5%	95%	1%	6%	93%	HF
5	1.5	-0.1	16 %	0%	84%	10%	0%	90%	HC
6	1.7	-3.0	7 %	2%	91%	4%	4%	92%	HF, HC
7	1.9	-2.6	12 %	1%	87%	9%	4%	87%	HF
8	2.0	-2.7	74 %	1%	25%	74%	2%	24%	HF, HC

During cooling to below 0℃, there was a general trend that the unfrozen pore water content decreased as the ice was formed, and the gas saturation slightly increased (Figure 3). During cooling below 0℃, not all pore water converted into ice. The amount of unfrozen pore water is dependent on temperature, sediment type, hydrate forming Gas and Gas pressure[50]. As temperature decrease from 0℃ to -3℃, amount of unfrozen water content decreased[5051]. The gas saturation increased from 2% to 4% in Experiment 6 and from 1% to 4% in Experiment 7. These new gas pockets were generated either due to the release of CH_4 from CH_4 saturated water as it crystallized

322 into ice or from liberated CH_4 when porous HF was destabilized and converted into ice. The CH_4
323 gas solubility in water decreases with decreasing temperature in the hydrate stability region [5253].
324 The cooling process could therefore trigger additional hydrate formation from dissolved CH_4 in
325 the water phase. However, the increase in CH_4 gas saturation during cooling, suggests that the
326 formation of ice was preferred over the formation of additional hydrates. Mechanisms such as the
327 expulsion of gas during water crystallization, trapped gas in low permeable rock, conversion into
328 hydrate, and extent of the hydrate stability zone due to loading by an ice sheet may cause pore gas
329 hydrate formation in permafrost [54]. Likelihood of methane gas presence in permafrost is higher [55],
330 and the presence of free methane in near-surface permafrost is reported previously [56].

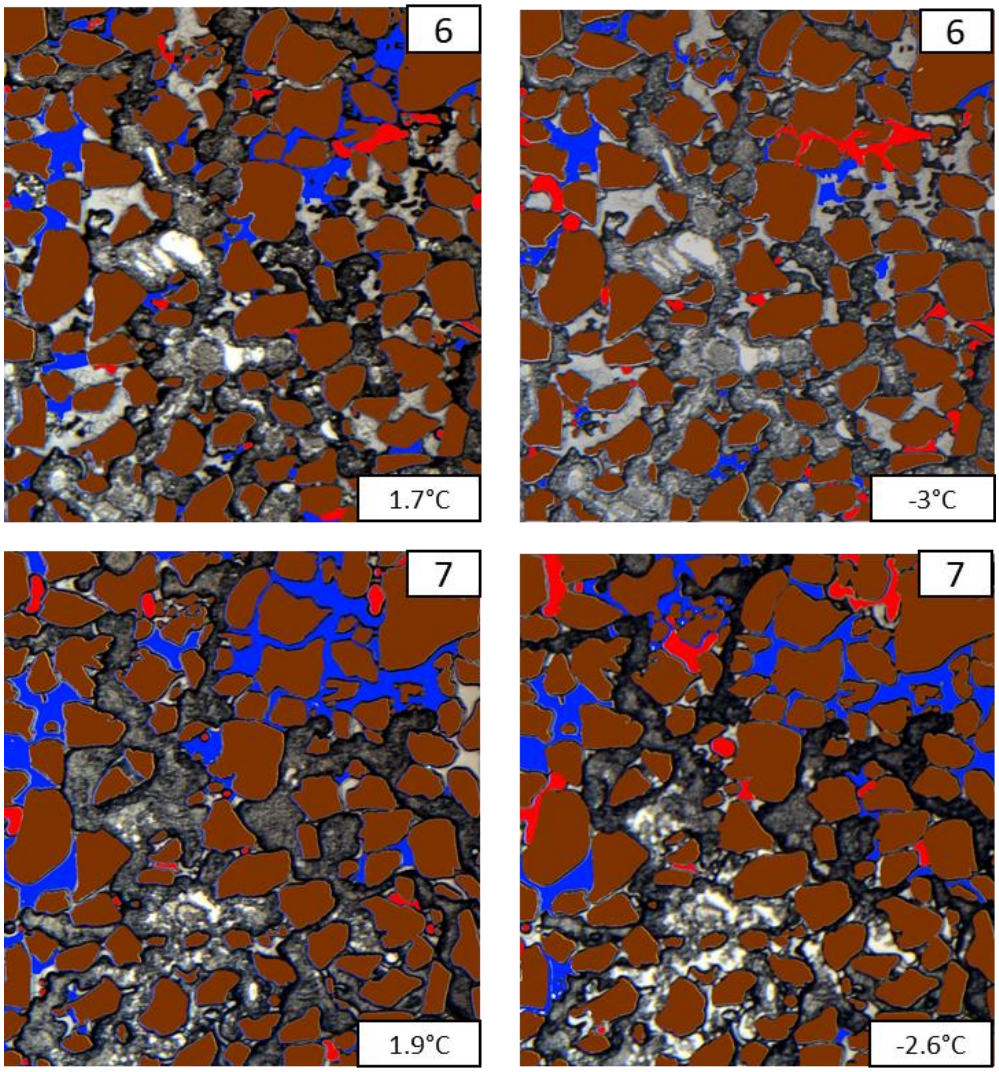

Figure 3 *Temperature-induced gas pocket development in Exp. 6 and 7 during cooling below 0°C. The silicon grains, liquid water, and gaseous CH_4 are coloured brown, blue, and red, respectively. The CH_4 gas hydrate phase is not segmented, and porous hydrate films (HF) are observed in dark grey and non-porous crystalline hydrates (HC) in transparent white. During cooling, new gas pockets (red) appeared, and the water saturation (blue) decreased. The amount of ice that formed during the cooling could not be inferred from the images.*

3.3. Effect of temperature on hydrate dissociation by pressure depletion

Hydrate dissociation during depressurization within porous media is influenced by heat transfer, mass transfer and intrinsic kinetics [57–59]. At the laboratory scale, kinetics and heat transfer

influence the dissociation behaviour whereas, at the field scale, the mass transfer via gas/water flow away from the hydrate dissociation front also influence the dissociation [59]. Overall, hydrate dissociation is characterized as endothermic process predominantly influenced by heat transfer due to the development of temperature gradient within the hydrate region during the dissociation [57].

3.3.1 Hydrate dissociation at constant T > 0°C

In this section, we have discussed the effect of hydrate morphology and its distribution within micromodel on the gas production behaviour during the dissociation at constant T >0°C. Dissociation through pressure depletion was conducted for three different hydrate saturation and distributions (Table 4).

Table 4 *includes experimental conditions for hydrate dissociation at constant T > 0°C. Pi denotes the pressure at the start of the dissociation. P1 denotes the pressure value at which dissociation/phase changes first occurred, and P2 is the pressure value at which the hydrate completely dissociate within FOV. Peq is calculated using CSMGem software for pure CH_4 gas hydrate at the given temperature. PM = Production method, DP = Depressurization, HM = Hydrate Morphology*

Exp	T (°C)	Before dissociation			HM	Pressure response (bars)				Δt (min)	PM
		S_W	S_g	S_H		P (bar)	P_{eq}	P_1	P_2		
1	0.9	1%	6%	93%	HF	85	28.4	27.58	22.75	46	DP
2	0.8	92%	0%	8 %	HC	76	28.1	19.50	14.12	135	DP
3	1.0	8%	3%	89%	HF, HC	60	28.7	18.30	15.98	61	DP

Experiment 1 had high hydrate saturation, S_H= 93%, and contained HF and free gas. Experiment 2 had low hydrate saturation, S_H=8%, and contained HC and pore water, while experiment 3 had high hydrate saturation, S_H= 88%, and contained HF, HC, and pore water within FOV. During pressure depletion, in each experiment, dissociation was observed at different pressures below the equilibrium pressure (P_{eq} ~ 28 bar).

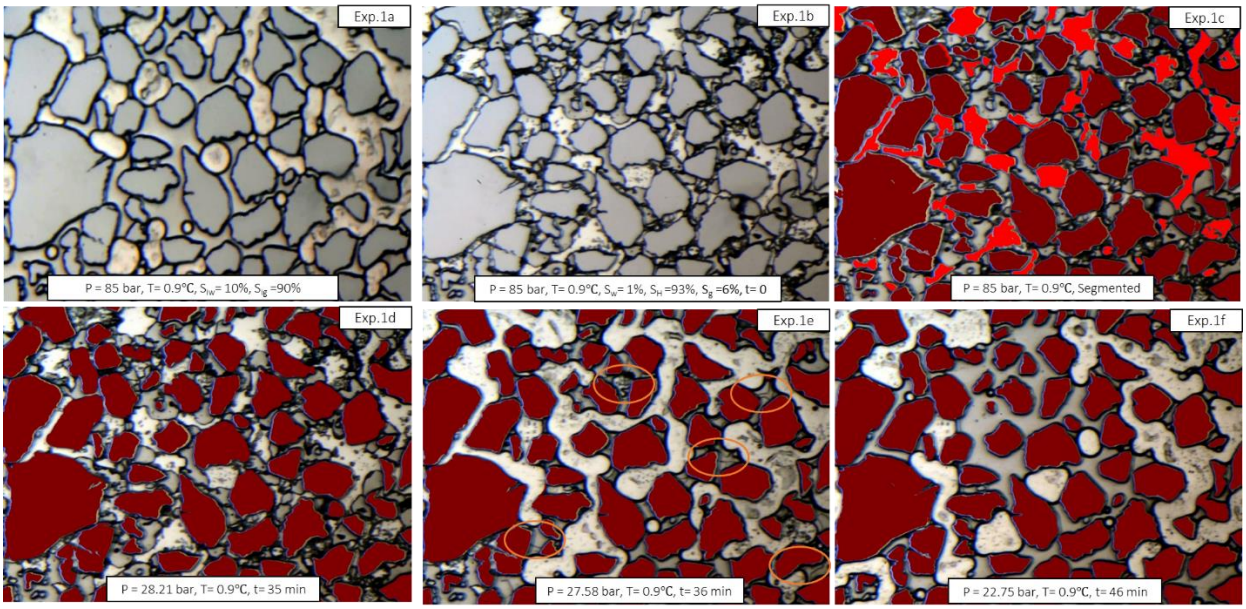

Figure 4 *Overview of the dissociation behaviour in Experiment 1. Dissociation temperature was 0.9°C, and the starting pressure was P = 85 bar. Dissociation was carried out at a constant flow rate of 10 ml/hours. Methane hydrate stability pressure is P = 28.4 bar at T =0.9 °C. Figure Exp.1a shows initial water and gas saturation before hydrate formation starts. FOV can be defined as low water and high gas saturation containing system. Figure Exp.1b displays the hydrate distribution and saturation at the start of the dissociation experiment. FOV displays high hydrate saturation containing HF and free gas saturation. Figure Exp.1c displays the segmented field of view, where red indicates the gas pockets. Figure Exp.1d is the status within the field of view (FOV) when pressure was reduced to 28.21 bar, after 35 minutes. No change in the field of view was observed. Figure Exp.1e shows the first dissociation point at P= 27.58 bar at t= 36 min shows HF melting. Figure Exp.1f shows complete dissociation at t=46 minutes at P=22.75 bar.*

Figure 4 illustrates the dissociation behaviour in experiment 1. FOV contains high hydrate saturation consists of HF (S_H= 93%) and free gas (6%). In experiment 1, HF started to dissociate immediately at P = 28.21 bar (refer to Figure Exp.1d) below $P_{eq\ (CH4)}$ = 28.4 bar due to porous nature and liberated Gas mobilized through the connected gas phase, leaving the hydrate film in contact with water. HF dissociated rapidly and from the centre of pore space towards pore walls and created a preferential pathway for fluid migration within hydrate distribution. Porous hydrates in excess gas environment experienced pressure response via connected gas phase, and the liberated CH_4 gas escaped the dissociation front via advective gas flow. Dissociation of HF formed

in narrow pore throats or in contact with water stopped temporarily, until gas invaded or expanded into pore throats from other parts of the micromodel, and contacted the hydrate (refer to Figure Exp.1e). Hydrate in FOV fully dissociated at P = 22.75 bar, approx. 6 bar below the hydrate stability pressure ((refer to Figure Exp.1f).

In contrast, in experiments 2 and 3, the first dissociation was observed at 19.5 bar and 18.3 bar, respectively, which is 9 bar and 10.4 bar below the equilibrium pressure. **Figure 5** displays the dissociation behaviour observed in experiment 2. The hydrate morphology was dominated by HC. FOV contained HC (S_H=8%) and pore water (S_w= 92%) (refer to Figure Exp.2b). Hydrate stability pressure P_{CH4}= 28.1 bar at T = 0.8 ℃. No change in FOV was observed when the pressure reached at P = 19.53 bar (refer to Figure Exp.2d). HC experienced pressure response via the water phase, and initial liberated CH_4 gas was trapped as immobile gas bubbles (figure Exp.2e and figure Exp.2f). The trapped gas bubbles started to mobilize when they achieved a critical size through coalescence with other nearby gas bubbles. A low hydrate saturation and the presence of free gas in the pores could accelerate the coalescence of the gas bubbles [32,33]. During pressure reduction, liberate gas from dissociation in adjacent pores invaded the field of view, displaced water from pore space and accelerated coalescence of isolated gas bubbles (refer to figure Exp.2f). In case of high hydrate saturations dominated by HC, the coalescence of gas bubbles would be slow due to shielding by non-porous hydrates. The dissociation front advanced through the pores dissociating HC in larger pore space while hydrate filled pores with narrow pore throats remained un-dissociated due to higher entry capillary pressure as the pressure response propagated to the next pore (refer to figure Exp.2h). Dissociation of HC in small pore throats occurred via methane gas molecule diffusion through the water phase. It is proposed that gas molecules from hydrate crystals diffuse through the water phase to the free gas phase in adjacent pore due to the methane

concentration gradient in water phase between free gas-water interface and water-hydrate interface. This gradient was caused by the difference in methane solubility in water phase due to the difference in temperature at two interface caused by endothermic hydrate dissociation [29].

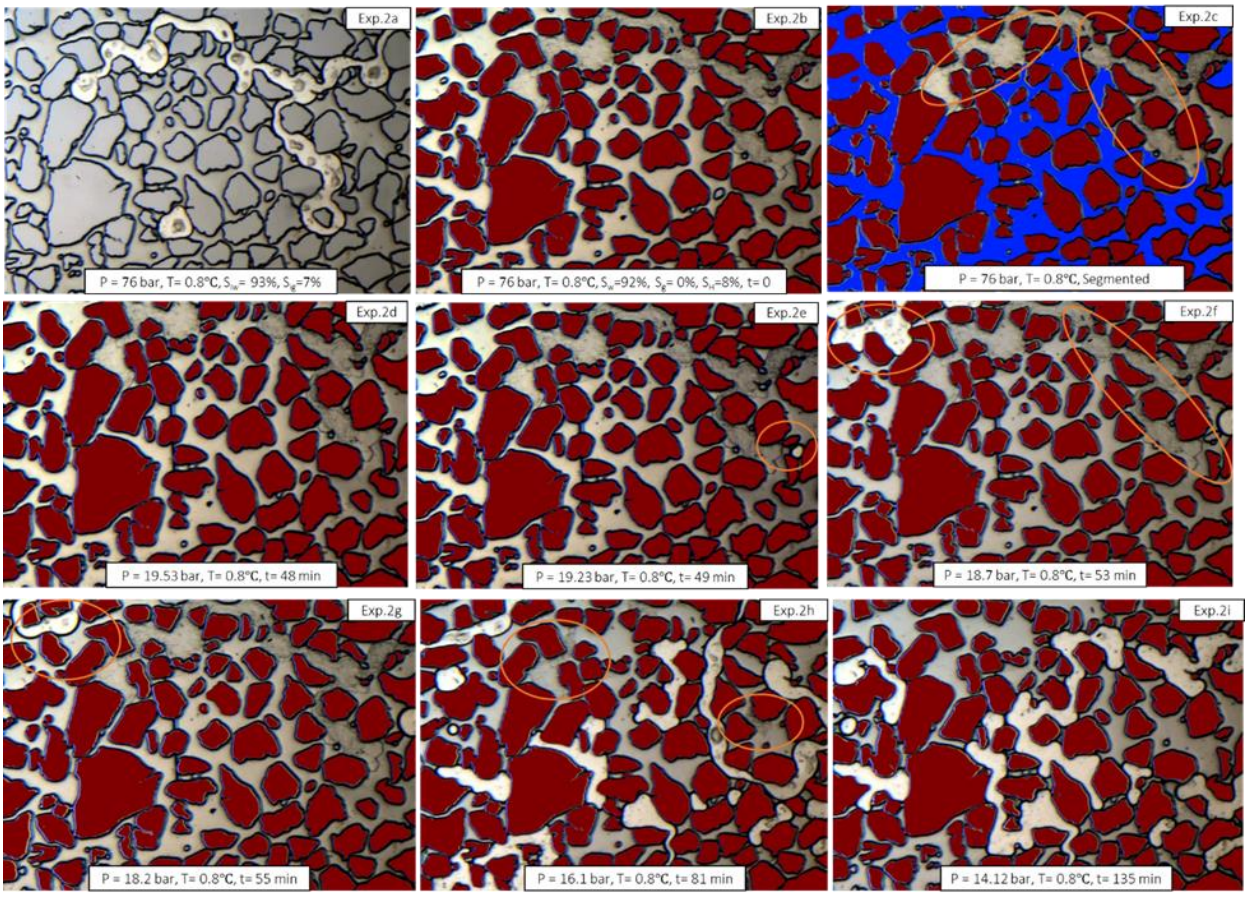

Figure 5 *Overview of the dissociation behaviour in experiment 2. Dissociation temperature was 0.8°C, and the starting pressure was P = 76 bar. Dissociation was carried out at a constant flow rate of 10 ml/hours. Figure Exp.2a display initial liquid water (W) and gas (G) saturation before hydrate formation. Figure Exp.2b display hydrate distribution before dissociation starts. Field of view includes crystalline hydrates (HC), water (W) and grains. Figure Exp.2c show segmented image. Blue colour indicates the presence of water and brown colour shows grains. HC are shown within the circle. No gas pocket was observed in the field of view. The starting saturation state is characterized as low hydrate saturation having HC surrounded by water in pore space. Figure Exp.2d is the status within the field of view (FOV) when pressure was reduced to 19.53 bar, after 48 minutes. No change in the field of view was observed. Figure Exp.2e shows the first dissociation point at P= 19.23 bar when the gas bubble appeared at t = 49 minutes. Figure Exp.2f shows the gas invasion from adjacent pores into the field of view displacing the water in pore space at P=18.7 bar, t= 53 minutes. Figure Exp.2g shows the gas dissolve back into water reflected by a decrease in gas saturation at t =*

55 minutes. Figure Exp.2h display invaded Gas-assisted HC dissociation at large pore space and stabilized HC in small pore throats, and free gas does not enter these pore throats. Figure Exp.2i shows the full dissociation at t=135 minutes at P=14.12 bar.

Due to endothermic cooling and Joule Thomson effect [60], immobile trapped gas bubbles could participate in secondary hydrate formation that would enhance the hydrate saturation within the pore space and reduce the relative permeability of the gas [61,62]. This could lead to gas pockets being temporarily trapped and surrounded by secondary hydrates. Delayed hydrate dissociation above 0°C due to extent and type of hydrate morphology can be described as hydrate self-preservation effect above 0°C. Makogon and Ghassemi [63] studied self-preservation for methane hydrate formed in freshwater above 0°C and suggested that self-preservation is caused by a change in pore space structure and size due to hydrate accumulation. Change in pore space geometry in the presence of hydrates increased the capillary pressure in pore space and reduced the water vapour pressure. In such cases, the gas production rate was a low, discontinuous and higher amount of energy needed to dissociate the hydrates in pore space. The pressure was depleted far below the equilibrium pressure before all the hydrates dissociated in the FOV.

Figure 6 below demonstrate the dissociation behaviour of hydrate system in experiment 3 having both HC and HF present within the field of view. FOV included high hydrate saturation (SH = containing HC, HF, pore water and CH_4 gas. Dissociation was carried out at constant temperature T = 1°C. When pressure arrived P = 18.3 bar, 10 bar below the hydrate stability pressure (P_{eq} = 28.7 bar), HF encapsulating the gas phase dissociated (refer to Figure Exp.3d). Hydrate film in all pores dissociated uniformly, and dissociation started from the middle of pore space. Heterogeneity in hydrate distribution and HF melting had created a preferential pathway within FOV for gas migration. HC in large pore space dissociated but gas remained trapped encapsulated by HF indicated by grey colour (refer to Figure Exp.3e). Dark-grey HF began to dissociate in pores when

in contact with the gas phase or when the size of gas inside these dark film achieve critical size (refer to Figure Exp.3f). Increase in gas saturation due to dissociation leads to invasion of gas into narrow pore throats against high capillary pressure and dissociate remained HC and HF. Hydrate in narrow pore throats was last to dissociate through the invasion of gas into pores and /or methane diffusion via connected liquid phase. (refer to Figure Exp.3j, Exp.3i)

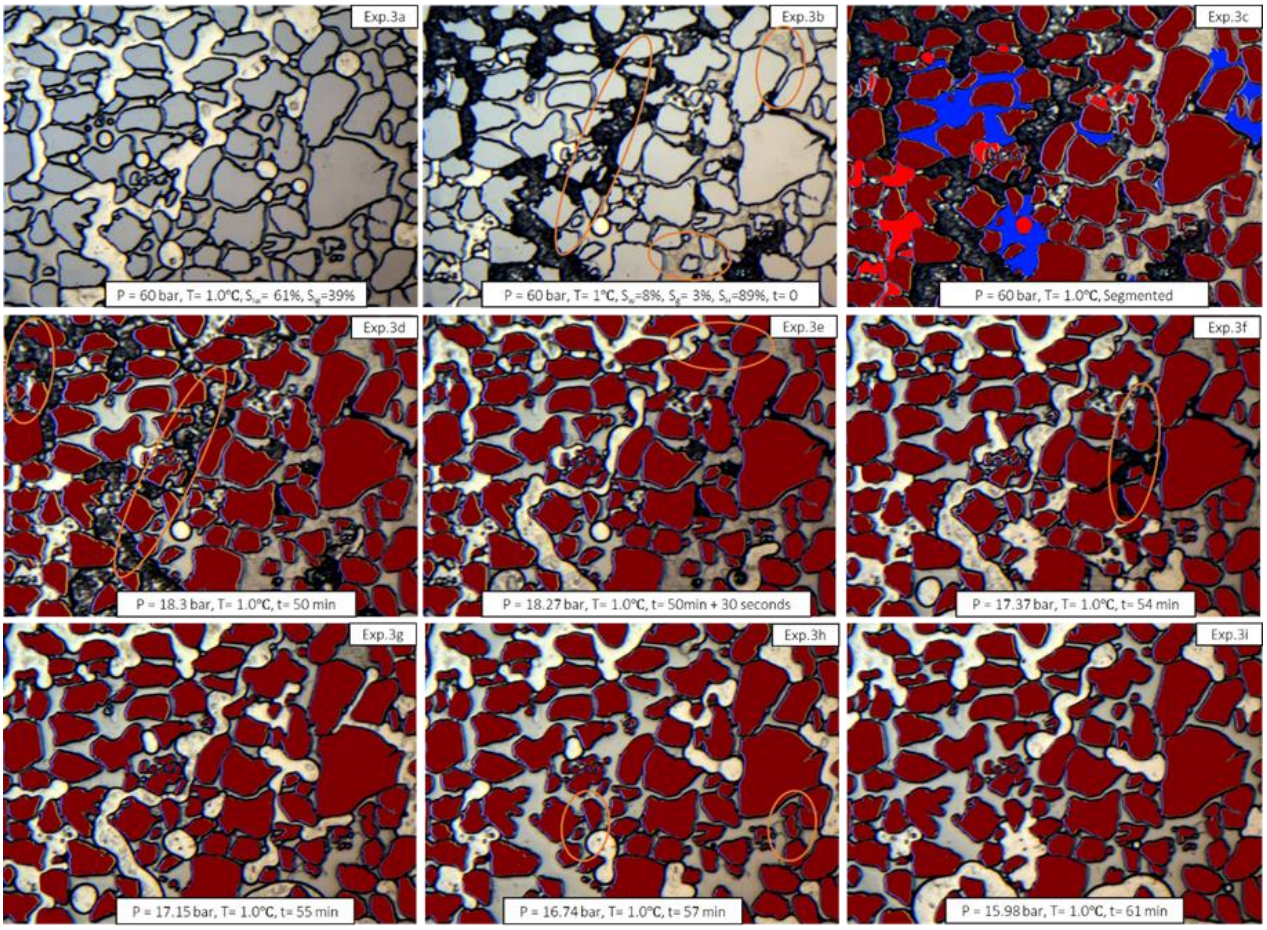

Figure 6 *Overview of the dissociation behaviour in experiment 3. Dissociation temperature was 1.0°C, and the starting pressure was P = 60 bar. Dissociation was carried out at a constant flow rate of 10 ml/hours—figure Exp.3a display initial liquid water (W) and gas (G) saturation before hydrate formation. Figure Exp.3b display hydrate distribution before dissociation starts. Field of view includes crystalline hydrates (HC), hydrae films (HF), water (W), Gas (G) and grains. HC and HF are identified within the circle. Figure Exp.3c show segmented image. Blue colour indicates the presence of water, red colour shows gas and brown colour shows grains. The starting saturation state is characterized as high hydrate saturation having HC, and HF surrounded by*

water and gas in the pore space. Figure Exp.3d showed hydrate film dissociation when pressure was reduced to 18.3 bar, after 50 minutes. Dissociation initiate at the centre of the pores. Figure Exp.3e shows complete dissociation of hydrate films, and liberated gas mobilized within pore space. Dissociation of HC adjacent to HF initiated. Figure Exp.3f shows the black colour hydrate films encapsulating liberated Gas from HC dissociation. Figure Exp.3g shows the liberated gas from black hydrate film dissociation expand to nearby HC present in narrow pore throats. Figure Exp.3h shows un-dissociated HC in pore throats dissociated by free gas or via methane gas diffusion through the water phase. Figure Exp.3i shows the full dissociation at t=61 minutes at P=15.98 bar.

The observations during this study reconfirm that porous hydrate and non-porous hydrate have distinctive dissociation behaviour that affects production rates of CH4 Gas [32,64]. The hydrate phase present in small pore throats is last to dissociate due to high capillary pressure. Hydrate dissociation is also accelerated in the presence of mobile free gas due to increased mass transfer and added convective heat flow to the overall heat transfer [27]. Endothermic nature of dissociation makes the mobility of gas phase in pore space an essential factor as immobile free gas act as heat insulator compare to water and restrict the heat transfer to the gas hydrate dissociation front thus lead to low dissociation rate. Heterogeneous hydrate saturation influence gas production rate such that gas recovery is slower for high hydrate saturation, and total gas produced is dependent on overall saturation [6547]. Simulation studies have also confirmed that gas production enhanced in the presence of free gas [66]. Therefore hydrate distribution with free gas presence would be an attractive target for gas production by pressure depletion. Recently, experimental studies show that hydrate specific surface area also control hydrate dissociation kinetics [67] such that surface coating hydrate dissociates faster than pore filling hydrates due to the higher specific surface area [68]. It is suggested that the hydrate surface area is a linear approximation of (hydrate volume)^2 during depressurization and (hydrate volume)^3 during thermal stimulation. Hydrate surface area is also proposed as a linear relationship of (hydrate volume)$^{2/3}$ for given hydrate saturation threshold [67].

3.3.2 Hydrate dissociation via depressurization at constant T < 0°C

In this section, we have discussed hydrate phase change during the pressure depletion at constant temperature T <0°C and the effect of heterogeneity in hydrate saturation within micromodel and dissociation temperature on the production rate and total production yield. (refer to table 4).

Table 5 *includes initial dissociation temperature (Td), initial hydrate/Ice saturation (SH/Sic), Initial starting pressure (P), Pressure at which the first dissociation observed (P1) and pressure at which hydrate fully dissociated (P2), Peq (CH_4) was calculated using CSM gem software, the total time during depressurization (Δt), Description of hydrate morphology pattern within field of view (FOV) and Dissociation method (DM). HM = Hydrate Morphology*

Exp	T_d(°C)	Before dissociation			HM	Pressure response (bars)				Δt (min)	DM
		S_{fw}	**S_{fg}**	**S_H/S_{ice}**		**P**	**P_{eq}**	**P_1**	**P_2**		
4	-0.5	1 %	6 %	93 %	HF	79	25.0	22.9	20.1	42	DP
7	-2.6	9 %	4 %	87 %	HF	55	23.4	15.5	14.4	89	DP
5	-0.1	10 %	0 %	90 %	HC	71	25.4	-	-	2846	DP+TS
6	-3.0	4 %	4 %	92 %	HF+HC	80	23.3	17.8	5.0	1115	DP+TS
8	-2.7	74 %	2 %	24 %	HF+HC	80	23.4	14.2	13.0	1450	DP+TS

Kinetics of methane hydrate dissociation below 0°C can be divided into two steps due to ice shielding mechanism.[69]. The first step includes melting of water lattice and desorption of methane molecule from the surface of the hydrate particle; the second step includes methane gas molecule migration towards the gas phase via diffusion through the ice sheet. The second step is the rate-determining step [70]. Table 5 describes the dissociation behaviour in experiments 4 and 7, carried out in the subzero temperature range (0 °C to -3 °C). We have discussed dissociation behaviour in Experiment 4 and experiment 7 together due to similar hydrate morphology at the start of hydrate dissociation. Experiments 4 and 7 had high saturations, S_H=93% in experiment 4 and S_H = 87% in experiment 7. In both cases, the hydrate saturation and morphology were very similar. Porous hydrates films HF were visible in FOV identified by their grey colour texture. FOV was also saturated with unfrozen pore water and gaseous CH_4 gas.

493 Figure 6 illustrates the dissociation sequence in experiment 4 under pressure depletion. FOV
494 contained HF was surrounded by the free gas phase, and small pores contained hydrate crystals
495 (refer to figure Exp.4b). Hydrate stability pressure is $P_{CH4 =}$ 25 bar at T = -0.5°C. At constant
496 production rate (10 mL/hour), the first instance of hydrate dissociation was observed at a pressure
497 of 22.9 bar indicated by uniform and rapid dissociation of HF which created preferential gas
498 migration pathway (refer to Figure exp.4e). The pressure at the first instance of dissociation was 2
499 bar below the dissociation pressure due to lower sensible heat availability from surrounding at T<
500 0°C. At the same time, hydrate crystals also dissociated indicated by a change in colour from
501 transparent to dark-grey. Liberate gas remained encapsulated in hydrate film (refer to Figure
502 exp.4f). As pressure further decreased, gas front arrived at HF, and Gas-assisted dissociation
503 happens due to enhance mass transfer caused by connecting the gas phase (refer to Figure exp.4g).
504 HF within narrow pore throats and smaller pore space were last to dissociate (refer to Figure
505 exp.4i) and hydrate fully dissociated at P = 20.1 bar after 42 minutes.

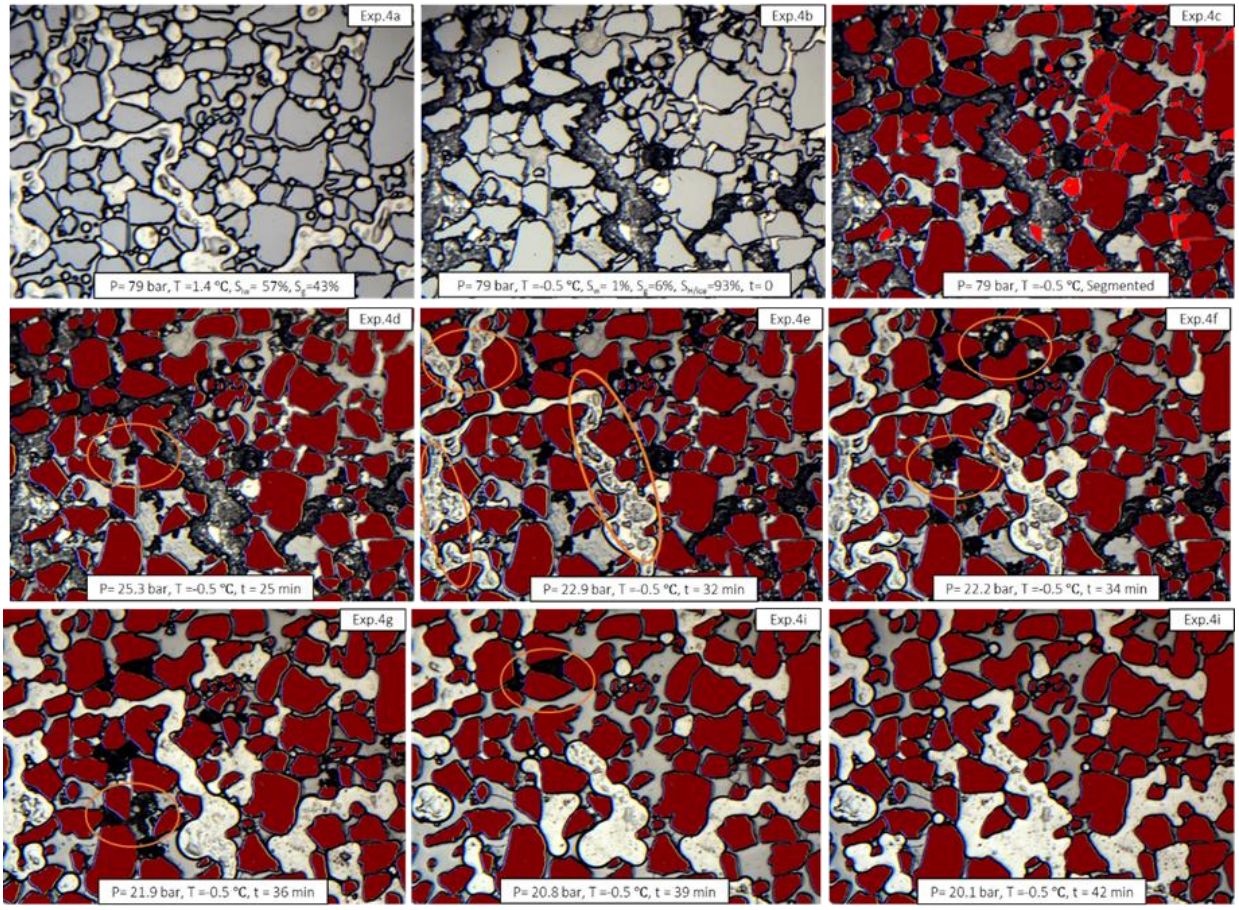

506

507 ***Figure 6*** *Overview of the dissociation behaviour of CH4 gas hydrate in experiment 4. Dissociation is carried out at -0.5°C in*
508 *experiment 4. Dissociation is carried out at a constant flow rate of 10 ml/hours. Figure Exp.4a display initial water and gas*
509 *saturation before hydrate formation. Figure Exp.4b show hydrate distribution and starting saturation state at P = 79 bar, T = -0.5*
510 *°C before dissociation starts. Figure Exp.4c shows the segmented field of view displaying grey hydrate film and gas pockets in red*
511 *colour. Figure Exp.4d display partial melting of HC indicated by the change in colour from white to grey. Figure Exp.4e displays*
512 *the first instance of hydrate dissociation at P= 22.9 bar. Figure Exp.4f displays hydrate melting initiation at different locations.*
513 *Figure Exp.4f to Figure Exp.4h displays hydrate melting, indicating continuous hydrate dissociation. Figure Exp.4i display full*
514 *hydrate dissociation within 42 minutes when pressure arrived at 20.1 bar. No hydrate and ice formation was observed*

515 Figure 7 illustrates the dissociation behaviour in experiment 7. FOV included dark-grey HF,
516 unfrozen pore water and trapped gas (refer to figure Exp.7b). Methane hydrate stability pressure
517 P_{CH4} is 23.4 bar at T = -2.6°C. As pressure started to go below stability pressure, trapped gas in
518 isolated pore space expanded with no distinctive dissociation until pressure arrived at P=15.5 bar

519 (refer to Figure Exp.7d and Exp.7e). Large pressure drop (ΔP = 8 bar) was required to dissociate
520 HF due to low sensible heat availability in surrounding as the temperature was -2.6℃. HF
521 dissociated rapidly and uniformly and created a preferential pathway for gas and liquid migration
522 (refer to Figure Exp.7f). Hydrate formed within narrow pore throats were last to dissociate as gas
523 was not able to invade into crystals due to high capillary pressure (refer to Figure Exp.7g).
524 Complete dissociation was observed at P = 14.4 bar after 89 minutes.

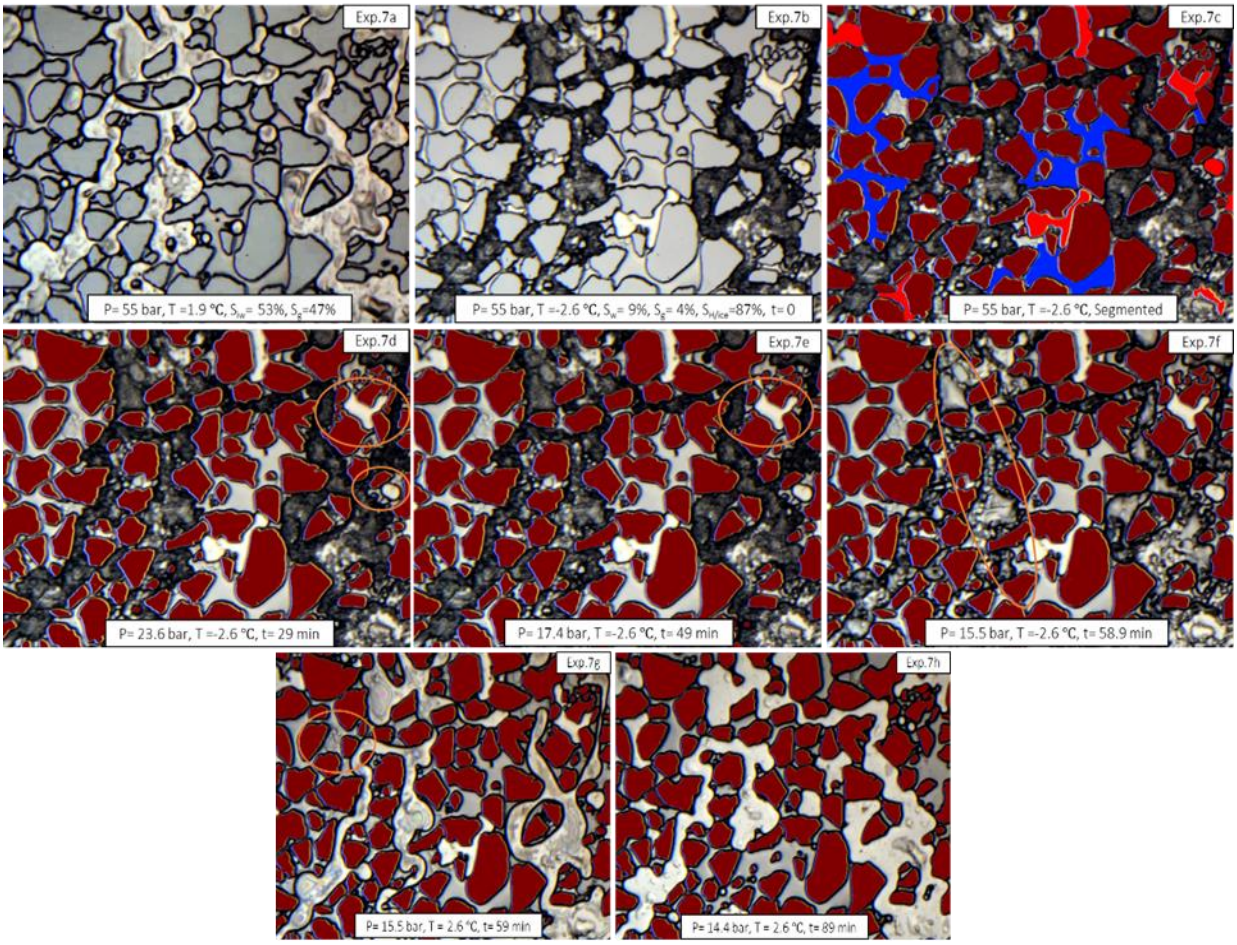

525

526 ***Figure 7*** *Overview of the dissociation behaviour of CH4 gas hydrate in experiment 7. Dissociation is carried out at -*
527 *2.6°C. Dissociation is carried out at a constant flow rate of 10 ml/hours. Figure Exp.7a display initial water and gas*
528 *saturation within the field of view before hydrate formation. Figure Exp.7b show hydrate distribution and starting*
529 *saturation state at P = 55 bar, T = -2.6 ℃ before dissociation starts. Figure Exp.7c shows the segmented field of view*

displaying grey hydrate film and gas pockets in red colour and water pocket in blue colour. Figure Exp.7d and Figure Exp.7d display partial dissociation indicated by an increase in gas saturation. Figure Exp.7e and Figure Exp.7f display the first instance of hydrate film dissociation at P= 15.5 bar after t= 59 minutes. Figure Exp.7g displays un-dissociated hydrates which fully dissociated at P =14.4 bar after t= 89 minutes, as shown in Figure Exp.7h. No hydrate and ice formation was observed

Dissociation behaviour in experiment 4 and experiment 7 illustrate that depressurization was sufficient to completely dissociate the hydrate, and no heating was required. No secondary hydrate formation was observed during the dissociation. Dissociation behaviour in experiments 4 and 7 can also be compared with experiment 1 due to similar hydrate morphology at the start of dissociation. All three experiments, hydrate morphology HF and some amount of HC at narrow pore throats. Presence of HF suggests high initial gas saturation and low initial water saturation. Depressurization was found to be sufficient to dissociate completely without combining with other techniques such as thermal stimulation. However, as dissociation temperature decreased from 0.9°C in experiment 1 to -2.6°C in experiment 7, a larger pressure drop was required below stability pressure to initiate the hydrate dissociation. For example, in experiment 1, hydrate started to dissociate at P = 27.58 bar, whereas in experiment 4, it started to dissociate at 22.9 bar and in experiment 7, it started to dissociate at P = 15.5 bar. This was due to lower sensible heat available in surrounding as temperature reduced.

Table 5 also provides information regarding the dissociation behaviour in experiments 5, 6 and 8. In experiment 5, dissociation was performed at -0.1 °C, whereas in experiments 6 and 8 dissociation experiments were performed at -3 °C approx. Hydrate distribution in experiments 5, 6 and 8 was different from experiments 4 and 7. In experiment 5, 6 and 8 hydrate saturation included a high volume of the non-porous and low volume of porous hydrate and had different

hydrate distribution than experiments 4 and 7. Hydrate saturation before dissociation in experiment 5, 6 and 8 was 90%, 92% and 24% respectively. In experiments 6 and 8 hydrates were surrounded by unfrozen pore water and trapped gas, whereas, in experiment 5, only unfrozen pore water was visible in FOV.

Figure 8 describes the hydrate dissociation behaviour in experiment 5. Dissociation was carried out by depressurization, followed by heating. Hydrate morphology within FOV included crystalline hydrates coexisting together with ice or unfrozen pore water. Due to the near similar refractive index, it was hard to differentiate hydrate from unfrozen water. Hydrate saturation could be described as high saturation ($S_{H/Ice}$ = 90%) calculated using image analysis. No gas pockets were visible within the field of view. During the pressure depletion at T = -0.1°C, hydrate crystals remained un-dissociated, and no partial dissociation or re-formation was observed when pressure arrived and remained at 12 bar for 1260 minutes (refer to Figure exp.5d). The pressure further reduced to 1 bar and remained stable at 1 bar for other 1620 minutes (refer to Figure exp.5e). According to CSMGem based calculation, methane hydrate stability pressure is around 25 bar at 1°C. No change within FOV was observed when methane hydrate remained outside its stability condition, confirming the strong self-preservation nature of pore-filling crystalline hydrate. Self-preservation was caused by crystalline hydrates reaching the metastable stage under subzero temperature in the presence of unfrozen pore water [71]. Another possibility could be ice formation in the model which obstructed the arrival of pressure response from the pump into the FOV. Due to the similar refractive index, unfrozen pore water and hydrate were not easily distinguished. Ice formation outside FOV was also not ruled out. Heating was used to dissociate hydrates in experiment 5 ultimately. During temperature increase, two major dissociation stage was observed within FOV. The first dissociation was observed below 0 °C suggesting melting of hydrate due to

their metastable nature below their stability pressure. Hydrate melting was confirmed visually based on the creation of gas pockets during heating (refer to Figure exp.5f). It was observed that no intermediate hydrate film formed unlike during pressure depletion stage and hydrate melted locally and rapidly creating liberated gas. As the heat was continued to supplied, gas volume expanded within FOV and Gas in contact with hydrate crystals initiated dissociation of HC. Gas-assisted HC dissociation involved two steps. In the first step, liberated gas was encapsulated by dark-grey HF and in the second step, full dissociation and gas liberation (refer to Figure exp.5f). Hydrate continued to dissociate either due to heat supply from beneath due to high thermal conductivity of silicon wafer or through Gas-assisted dissociation (refer to Figure exp.5g). Hydrate in small pore space and narrow pore throats remained intact. Second rapid and uniform melting was observed at 0.5℃ (refer to Figure exp.5h). Remained hydrate in narrow pore throats dissociated as the temperature reached T = 0.6℃ (refer to Figure exp.5i). No hydrate re-formation was observed during the heating. Experimental study on the dissociation behaviour of frozen hydrate-bearing sediments by temperature increase suggested that hydrate dissociates before the pore ice melting and critical temperature sufficient for gas hydrate dissociation varies from -3℃ to -0.3℃ and depends on particle size and salinity of the water [71].

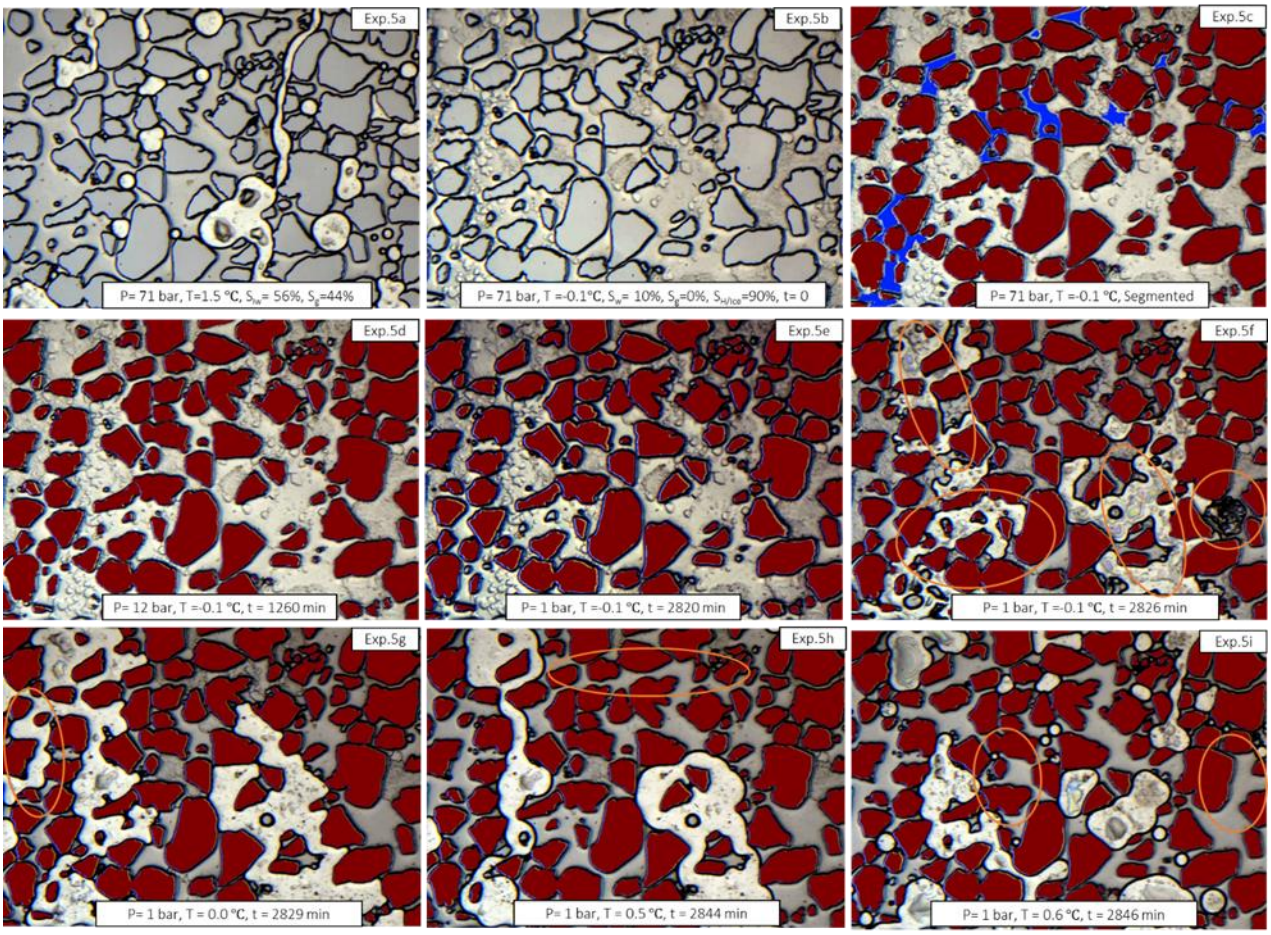

Figure 8 *Overview of the dissociation behaviour in experiment 5. Dissociation temperature was -0.1°C, and the starting pressure was P = 71 bar. Dissociation was carried out at a constant flow rate of 10 ml/hours. Figure Exp.5a displays initial water and gas saturation within the field of view before hydrate formation. Figure Exp.5b show hydrate morphology and distribution at P = 71 bar, T = -0.6 °C at the start of dissociation. Figure Exp.5c shows the segmented field of view displaying transparent HC, Ice and water pocket in blue colour. Figure Exp.5d and Exp.5e display the field of view (FOV) at P=12 bar after 1260 minutes and at P= 1 bar after 2820 minutes. No change in the field of view observed due to strong self-preservation below subzero temperature. Figure Exp.5f to Figure Exp.5i display the dissociation behaviour during heating. Figure Exp.5f display the first instance of HC dissociation at multiple places within FOV, 6 minutes after the heating started. HC dissociation was rapid and liberated gas expanded and invaded into pore space, accelerated and assisted the HC dissociation in the vicinity due to connected gas phase as shown in Exp.5g. As the temperature continues to increase and arrived above 0°C, Figure Exp.5h shows second hydrate dissociation above 0 °C at T=0.5°C. HC in narrow pore throats and small pore space dissociated in the end at T=0.6°C.*

Experiments 4 and 5, had a similar dissociation temperature but had different dissociation behaviour. Initial FOV in during both experiments contained a similar amount of hydrate

606 saturation (S_H=87%-93%) but differ in hydrate morphology and hydrate distribution. Hydrate
607 morphology in experiment 4 included HF and visible gas pockets, whereas hydrate morphology in
608 experiment 5 included HC and unfrozen pore water. Pressure depletion was sufficient in
609 experiment 4 but not in experiment 5 due to high self-preservation shown by HC in the presence
610 of unfrozen pore water. Thus the difference in dissociation behaviour is attributed to the difference
611 in hydrate morphology and the amount of unfrozen pore water.

612 Dissociation behaviour during experiments 6 and 8 had similar characteristic hence discussed
613 together. Experiments 6 and 8 both had similar hydrate morphology having both porous hydrate
614 film and non-porous crystalline hydrates within FOV at the start of the hydrate dissociation.
615 Experiments 6 and 8 also had near similar dissociation temperature at -3°C and -2.7°C respectively.
616 Figure 9 describes the dissociation behaviour in experiment 6. The pressure at the start of the
617 dissociation was 80 bar, and the temperature was -3°C. During the pressure depletion, when
618 pressure arrived below hydrate stability pressure ($P_{eq}CH_4$ equal to 23.1 bar) no change in the
619 hydrate morphology was observed when pressure reduced to 17.8 bar after 60 minutes (refer to
620 figure Exp.6d). As pressure depletion continued further, quick rearrangement within the field of
621 view was observed after 36 seconds (refer to figure Exp.6e). Rearrangement was identified by HF
622 colour change into a dark colour, suggesting a change in hydrate film thickness followed by
623 crystallization of unfrozen pore water identified by white colour (refer to figure Exp.6f). This
624 process was quick and finished within 1 minute at P = 17.3 bar. Further pressure depletion did not
625 lead to any significant redistribution within the field of view as pressure reduced to 13.7 bar (refer
626 to figure Exp.6g). As pressure continued to decrease and reached 5 bar, HF thickness reduced from
627 the centre of pore space towards pore wall and liberated gas remained trapped due to high
628 saturation and low permeability (refer to figure Exp.6i). When the pressure remained constant at

5 bar for next 840 minutes, we observed an increase in gas saturation. Increase in gas saturation was caused due to enhanced ability of gas molecules to diffuse through hydrate film as hydrate films were much thinner at lower pressure compared to a higher pressure (refer to figure Exp.6j). Released gas remained trapped due to blocking of pore space caused by the presence of hydrates and ice. Hydrates remained stable in narrow pore throats and FOV contained low hydrate saturation and high hydrate saturation. To fully dissociate the hydrates, ambient heating was used. Heat transported into micromodel from beneath and uniformly dissociated hydrate due to high thermal conductivity of silicon wafer when the temperature reached to T=-0.9°C (refer to Figure Exp.6k). Hydrate fully dissociated as shown at temperature T= -0.7°C (refer to Figure Exp.6r). No hydrate re-formation was observed during the heating and hydrate melted uniformly. All hydrate dissociated much below 0°C indicating no presence of ice within FOV at the start of dissociation.

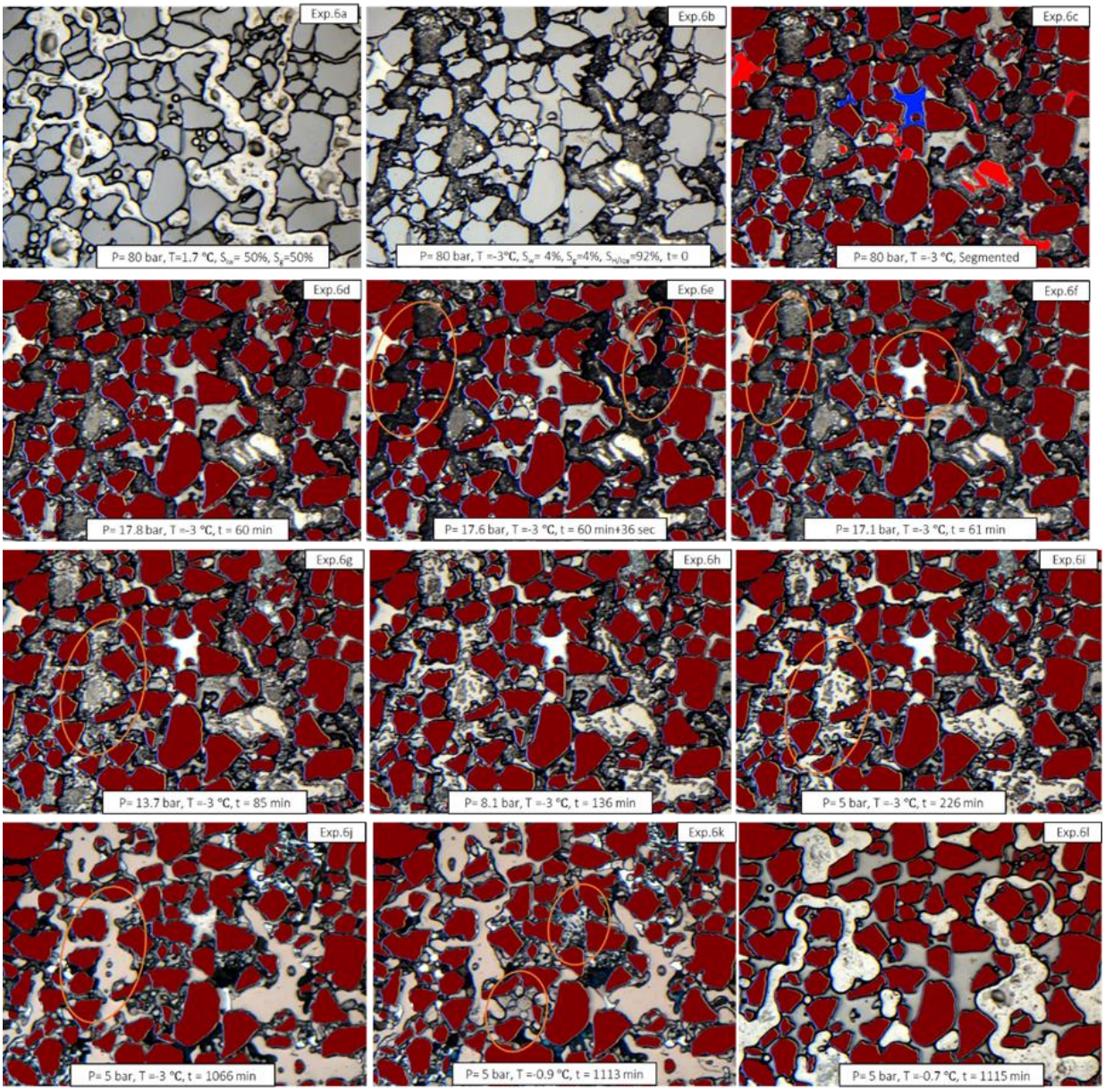

640

641 ***Figure 9*** *Overview of the dissociation behaviour in experiments 6. CH_4 stability pressure (P) is equal to 23.3 bar at T = -3°C*
642 *(CSMGem). Dissociation was carried out at a constant pump retraction at a flow rate of 10 ml/hours. Figure Exp.6a displays*
643 *initial water and gas saturation within the field of view before hydrate formation. Figure Exp.6b show hydrate morphology and*
644 *distribution at P = 80 bar, T = -3.0 °C at the start of dissociation. Figure Exp.6c segmented field of view displaying transparent*
645 *black-grey HF, unfrozen pore water in blue and isolated gas pockets in red. Figure Exp.6d shows the field of view after 60 minutes*
646 *at P =17.8 bar, Figure Exp.6e, Exp.6f displays phase change at constant pressure identified by crystallization of unfrozen pore*
647 *water into ice (circled in Exp.6f) and change in hydrate film thickness. Figure Exp.6g, Exp.6h and Exp.6i show trapped gas pocket*
648 *creation due to retarded melting of hydrae films at the centre of pores when pressure reduced from 13.7 bar to 5 bar. Trapped gas*

remained immobile at P= 5 bar for next 840 minutes, as shown in figure Exp.6j. Field of view included low hydrate saturation and high gas saturation at T = -3℃. Hydrate films remain stable at narrow pore throats and smaller pore space due to hydrate self-preservation at -3℃ in the presence of ice. The ambient heating technique was used to dissociate hydrates. Heat transported into micromodel from beneath and uniformly dissociated hydrate due to high thermal conductivity of silicon wafer. Figure Exp.6j show melting of ice and hydrate dissociation at T = -0.9℃. Hydrate fully dissociated, as shown in Figure Exp.6r at temperature T= -0.7℃. No hydrate re-formation was observed during the heating and hydrate melted uniformly.

Figure 10 illustrates the dissociation behaviour in experiment 8. The pressure at the start of the dissociation was 80 bar and temperature was -2.7 ℃. Hydrate saturation was low and included porous hydrate film HF in dark-grey colour and transparent HC. Most of FOV included unfrozen pore water. The presence of ice within FOV could not be confirmed. During pressure depletion under constant pump flow rate retraction (10 ml/h), the first instance of hydrate dissociation was observed at P = 14.2 bar identified by uniform melting of HF (refer to figure Exp.8d). Hydrate dissociation occurred 9 bar below the methane hydrate stability pressure P = 23.4 bar at T= -2.7℃ caused by low sensible heat availability below subzero temperature [72]. Thereafter, ice formation and secondary hydrate formation was observed. Ice crystallized from unfrozen pore water and identified in white colour and the second hydrate formed in smaller pore space and narrow pore throats identified in dark-grey colour (refer to figure Exp.8g). Secondary hydrate stability in pore space was driven by capillary pressure variation due to pore space geometry and local pressure and temperature conditions in pore space. Secondary hydrate stability was further enhanced by self-preservation effect in the presence of ice in the surrounding. Liberated gas from retarded dissociation of hydrate film remain trapped and expanded the gas volume already present in pore space at 5 bar pressure(refer to figure Exp.8i). Unfrozen pore water and liberated water from the HF melting in pore space also participated in the ice formation and secondary hydrate formation, thus improved the self- preservation during the dissociation process [7313].

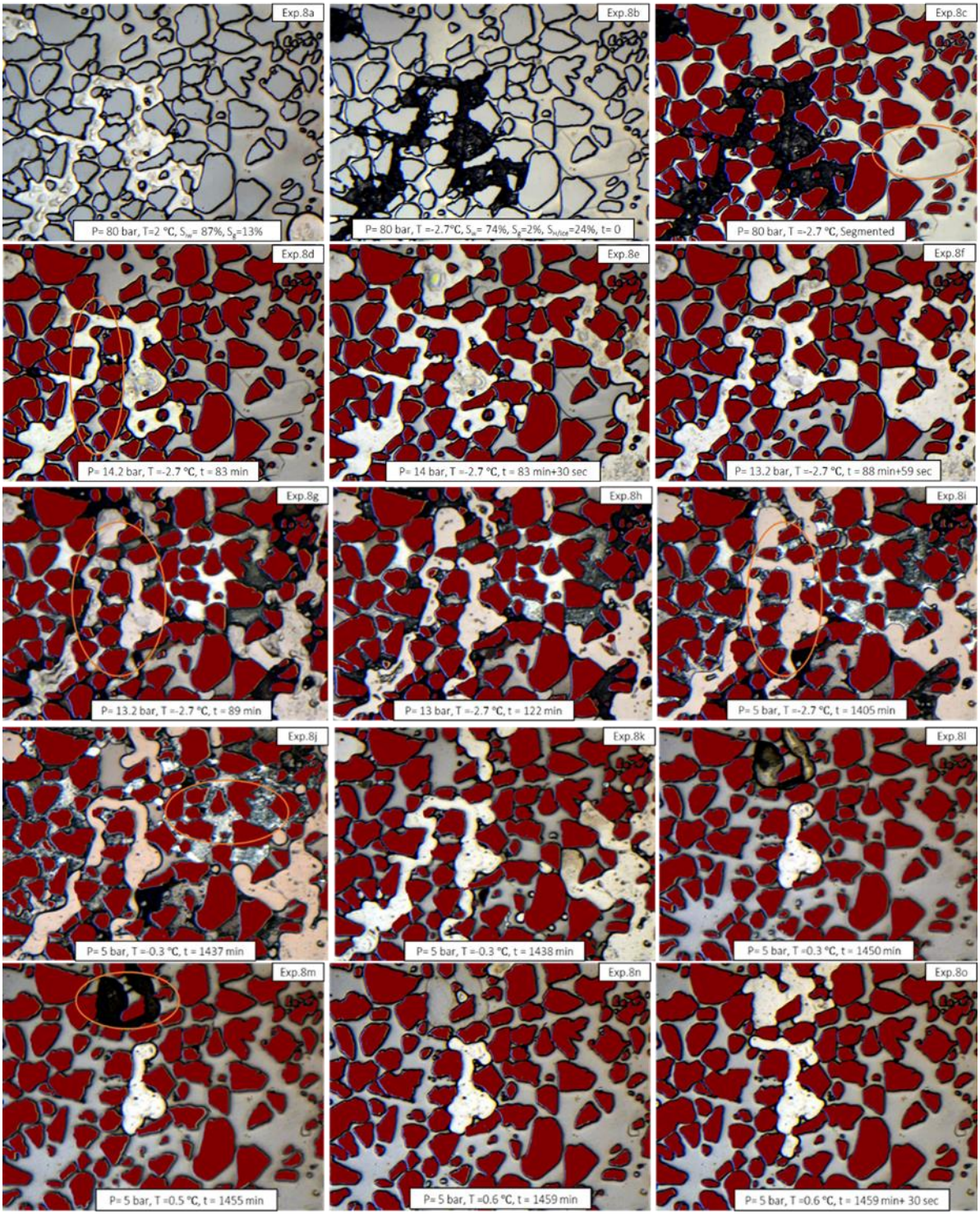

673

674 ***Figure 10*** *Overview of the dissociation behaviour in experiment 8. CH_4 hydrate stability pressure (P) is equal to 23.4 bar at T=-*

675 *2.7°C (CSMGem). Figure Exp.8a displays initial water and gas saturation within the field of view before hydrate formation. Figure*

676 *Exp.8b show hydrate morphology and distribution at P= 80 bar, T= -2.7 °C at the start of dissociation. Figure Exp.8c shows the*

segmented field of view displaying black-grey HF, transparent HC and unfrozen pore water in blue. Field of view is characterized as low hydrate saturation having heterogeneous distribution and high saturation of unfrozen pore water. Figure Exp.8d and Exp.8e shows the first instance of hydrate film melting followed by an invasion of Gas within FOV from surrounding pore space at 14 bar pressure. Figure Exp.8f, Exp.8g shows re-formation process occurred at 13.2 bar. Field of view in figure Exp.8g included trapped gas pockets, ice from unfrozen pore water crystallization and black-grey film. Figure Exp.8h shows the field of view after 122 minutes when P = 13 bar. Exp.8i shows the field of view at P= 5 bar after 1405 minutes. FOV included expanded gas volume trapped in pore space due to pore space blocking caused by ice formation. Figure Exp.8j – Figure Exp.8o shows dissociation behaviour under heating. Figure Exp.8j-Exp.8k shows the field of view at T= -0.3℃. FOV shows homogenous ice melting within pore space as ambient heat supplied from beneath the hydrate due to high thermal conductivity of silicon wafer. Figure Exp.8l-Exp.8n shows the hydrate re-formation and dissociation during the heating process above T >0 ℃ and P=5 bar, which lasted for 10 minutes. During the hydrate re-formation, water in pore space encapsulated gas pocket as HF which converted into a crystalline form. Exp.8n show HC in pore space which was unstable and quickly dissociated, as shown in Figure Exp.8o at T=0.6℃.

Re-formation involving secondary hydrate formation and ice formation is characteristically different from hydrate formation due to its shorter induction time [74] and can be identified due to large rearrangement within FOV within a short period. Risk of re-formation was higher in the presence of unfrozen pore water in the vicinity. The sensible heat of hydrate, heat supply from the sediment grains and pore fluid and heat transport from surrounding though conduction and advection were not sufficient for the heat required for endothermic dissociation during depressurization [75]. The re-formation process further reduced the in situ permeability and obstruct the gas migration as gas pockets were trapped and shielded by ice and hydrate. Secondary hydrate formation was also visually observed in other experimental studies [60,76]. Ice formation enhanced self-preservation of hydrates and acted as a solid protective shield around hydrate to stop it from further dissociation by reducing the heat transfer from the surrounding. Transport of liberated CH_4 Gas from dissociation was limited to diffusion through the ice sheet. Reformation had made depressurization ineffective, and FOV remained unchanged when the micromodel was kept at very low pressures for more than 48 hours.

Experiments 6, 7 and 8 had near similar dissociation temperature and have depressurized under the same flow rate (10 ml/hour) however, no ice formation and secondary hydrate formation was observed in experiment 7. This could be due to the low amount of unfrozen pore water, and gas dominated hydrate saturation that had assisted in gas production and reduced the risk of secondary hydrate formation and ice formation. Risk of re-formation also increased as the temperature changed to -3℃ as sensible heat supply decreased during the depressurization at the lower temperature.

The pressure drop required to initiate hydrate dissociation in experiments 5, 6 and 8 was much higher than experiments 4 and 7. Non-porous hydrate crystals were more stable than porous hydrates during the depressurization, and depressurization was not sufficient to dissociate hydrates. During pressure depletion, the re-formation was observed, and hydrate remains un-dissociated due to self-preservation property. Experiments 5, 6 and 8, self-preserved, un-dissociated hydrates were dissociated using thermal stimulation. Thermal stimulation is considered as an effective technique to address insufficient heat supply, avoid ice generation and formation of the secondary hydrate. Thermal stimulation increase temperature and supply essential heat during endothermic dissociation and cooling due to Joule Thomson Effect. In literature, different heat supply methods have been proposed, including microwave stimulation, warm water injection, thermal huff and puff and heat transfer from overburden or underlying units [77].

3.3.3 Self preserved hydrate dissociation via heating

Thermal stimulation via ambient heating was used to dissociate hydrate in experiment 5, 6 and 8 entirely. Hydrate dissociation during heating was uniform compared to pressure depletion. During the heating, heat supplied distributed among hydrate dissociation, temperature increase and energy

change due to outflow to the pump. Hydrate dissociation and reformation is the function of injection heat, heat transfer, mass transfer and hydrate saturation [5].

Hydrate dissociated from beneath and uniformly due to the high thermal conductivity of the silicon wafer. Simulation studies show that production performance correlate with deposit temperature and increase in 1℃ temperature of deposits could lead to 8 times increase in production rate due to an increase in sensible heat available for dissociation. Thermal stimulation can provide additional heat to compensate heat loss during the depressurization, remove unwanted ice and secondary hydrate formation leading to unblocking the pore space[78]. However, when this technique is used, stand-alone, would require excessive energy and have low production rate [79]. Studies show that warm water injection is preferred over ambient heating to achieve higher gas production yield as injected water would displace the gas from pore space[77].

During the heating in experiment 8, metastable secondary hydrate dissociated first at T <0℃ as the heat was supplied into micromodel through the ambient heating method. Hydrate dissociation identified by a decrease in black film area and increase in pore water (refer to figure Exp.8j) has enabled gas migration within pore space. Not all secondary hydrate dissociated during heating below 0℃ suggest stability of secondary hydrate was driven by self-preservation as well as pore-scale factors such as capillary pressure, hydrate filled pore space geometry and local temperature. As the heat was continued to supply, uniform ice melting was observed across pore space below 0 ℃ lead to gas and water migration within pore space (refer to figure Exp.8k). Some un dissociated secondary hydrate dissociated as the temperature reached above 0℃. As Temperature continues to increase, hydrate re-formation was observed at T = 0.3℃ (refer to figure Exp.8l) due to thawing of porous ice that did not turn into hydrate [80]. Re-formation during heating included hydrate film encapsulating the gas which later crystallized in the presence of pore water at T = 0.6℃ (refer to

748 figure Exp.8n). Hydrate re-formation was temporary and hydrate dissociated uniformly and
749 homogenously at T = 0.6°C (refer to figure Exp.8o).

750 **4. Conclusions**

751 Permafrost gas hydrate sediments can be characterized as sediments containing non-uniformly
752 distributed gas pockets below the 0°C in equilibrium with unfrozen pore water, hydrate and ice.
753 Understanding of quantity and quality of initial hydrate saturation is very critical for the selection
754 of correct production techniques in the permafrost region as hydrate dissociation behaviour during
755 pressure depletion depends on heterogeneity in hydrate distribution (porous/non-porous hydrate),
756 temperature, and presence of unfrozen pore water. At subzero temperature, delayed hydrate
757 dissociation under pressure depletion was observed due to lower sensible heat and higher self-
758 preservation in the presence of unfrozen pore water. Hydrate self-preservation was further
759 enhanced due to ice formation and/or secondary hydrate formation during pressure depletion
760 driven by the amount of unfrozen pore water. In the presence of free gas and the absence of
761 unfrozen pore water, the risk of re-formation reduced. Direct visualization suggests that
762 depressurization combined with thermal stimulation technique is an efficient technique for gas
763 production from high and low hydrate saturation reservoir in permafrost due to its ability to
764 unblock pores, melt secondary hydrate and improve permeability to enhance total gas yield and
765 gas production rate. Results suggest that initial information about hydrate saturation and free gas
766 availability is essential in selecting the correct production technique.

767

768 **Corresponding Author**

*Correspondence: Jyoti Shanker Pandey (jyshp@kt.dtu.dk) & Geir Ersland (geir.ersland@uib.no)

Author Contributions: Conceptualization, investigation, data analysis, original draft preparation, review and editing JSP, Review: SA, review NVS, and Project administration / Funding acquisition, GE

Funding:

Conflicts of Interest: The authors declare no conflict of interest.

References

(1) Sloan, E. D.; Koh, C. A.; Koh, C. *Clathrate Hydrates of Natural Gases*, Third Edit.; CRC Press., 2007.

(2) Boswell, R.; Collett, T. S. Current Perspectives on Gas Hydrate Resources. *Energy Environ. Sci.* **2011**, *4* (4), 1206–1215. https://doi.org/10.1039/c0ee00203h.

(3) Chong, Z. R.; Yang, S. H. B.; Babu, P.; Linga, P.; Li, X. Sen. Review of Natural Gas Hydrates as an Energy Resource: Prospects and Challenges. *Appl. Energy* **2016**, *162*, 1633–1652. https://doi.org/10.1016/j.apenergy.2014.12.061.

(4) Waite, W. F.; Kneafsey, T. J.; Winters, W. J.; Mason, D. H. Physical Property Changes in Hydrate-Bearing Sediment Due to Depressurization and Subsequent Repressurization. *J. Geophys. Res. Solid Earth* **2008**, *113* (7), 1–12. https://doi.org/10.1029/2007JB005351.

(5) Yang, M.; Zhao, J.; Zheng, J.; Song, Y. Hydrate Reformation Characteristics in Natural Gas Hydrate Dissociation Process: A Review. *Appl. Energy* **2019**, *256* (September), 113878. https://doi.org/10.1016/j.apenergy.2019.113878.

(6) Collett, T. S.; Dallimore, S. R. Permafrost-Associated Gas Hydrate. In *Natural Gas Hydrate: In Oceanic and Permafrost Environments*; Max, M. D., Ed.; Springer Netherlands: Dordrecht, 2003; pp 43–60. https://doi.org/10.1007/978-94-011-4387-5_5.

(7) Chen, D. F.; Wang, M. C.; Xia, B. Formation Condition and Distribution Prediction of Gas Hydrate in Qinghai-Tibet Plateau Permafrost. *Acta Geophys. Sin.* **2005**, *48* (1), 165–172. https://doi.org/10.1002/cjg2.638.

(8) Moridis, G. J.; Reagan, M. T. Estimating the Upper Limit of Gas Production from Class 2 Hydrate Accumulations in the Permafrost: 1. Concepts, System Description, and the Production Base Case. *J. Pet. Sci. Eng.* **2011**, *76* (3–4), 194–204. https://doi.org/10.1016/j.petrol.2010.11.023.

(9) Chuvilin, E.; Bukhanov, B.; Davletshina, D.; Grebenkin, S.; Istomin, V. Dissociation and Self-Preservation of Gas Hydrates in Permafrost. *Geosciences* **2018**, *8* (12), 431. https://doi.org/10.3390/geosciences8120431.

(10) Chuvilin, E. M.; Yakushev, V. S.; Perlova, E. V. Gas and Possible Gas Hydrates in the Permafrost of Bovanenkovo Gas Field, Yamal Peninsula, West Siberia. *Polarforschung* **2000**, *68* (1–3), 215–219.

(11) Kuhs, W. F.; Genov, G.; Staykova, D. K.; Hansen, T. Ice Perfection and Onset of Anomalous Preservation of Gas Hydrates. *Phys. Chem. Chem. Phys.* **2004**, *6* (21), 4917–4920. https://doi.org/10.1039/b412866d.

(12) Takeya, S.; Ripmeester, J. A. Anomalous Preservation of CH4 Hydrate and Its Dependence on the Morphology of Hexagonal Ice. *ChemPhysChem* **2010**, *11* (1), 70–73. https://doi.org/10.1002/cphc.200900731.

(13) Ershov, E. D.; Yakushev, V. S. Experimental Research on Gas Hydrate Decomposition in Frozen Rocks. *Cold Reg. Sci. Technol.* **1992**, *20* (2), 147–156. https://doi.org/10.1016/0165-232X(92)90014-L.

(14) Stern, L. A.; Circone, S.; Kirby, S. H.; Durham, W. B. Temperature, Pressure, and Compositional Effects on Anomalous or "Self" Preservation of Gas Hydrates. *Can. J. Phys.*

2003, *81* (1–2), 271–283. https://doi.org/10.1139/p03-018.

(15) Stern, L. A.; Circone, S.; Kirby, S. H.; Durham, W. B. Anomalous Preservation of Pure Methane Hydrate at 1 Atm. *J. Phys. Chem. B* **2001**, *105* (9), 1756–1762. https://doi.org/10.1021/jp003061s.

(16) Takeya, S.; Ebinuma, T.; Uchida, T.; Nagao, J.; Narita, H. Self-Preservation Effect and Dissociation Rates of CH4 Hydrate. *J. Cryst. Growth* **2002**, *237–239* (1-4 I), 379–382. https://doi.org/10.1016/S0022-0248(01)01946-7.

(17) Takeya, S.; Uchida, T.; Nagao, J.; Ohmura, R.; Shimada, W.; Kamata, Y.; Ebinuma, T.; Narita, H. Particle Size Effect of CH4 Hydrate for Self-Preservation. *Chem. Eng. Sci.* **2005**, *60* (5), 1383–1387. https://doi.org/10.1016/j.ces.2004.10.011.

(18) Zhong, J. R.; Zeng, X. Y.; Zhou, F. H.; Ran, Q. D.; Sun, C. Y.; Zhong, R. Q.; Yang, L. Y.; Chen, G. J.; Koh, C. A. Self-Preservation and Structural Transition of Gas Hydrates during Dissociation below the Ice Point: An in Situ Study Using Raman Spectroscopy. *Sci. Rep.* **2016**, *6* (December), 1–13. https://doi.org/10.1038/srep38855.

(19) Takeya, S.; Ripmeester, J. A. Dissociation Behavior of Clathrate Hydrates to Ice and Dependence on Guest Molecules. *Angew. Chemie - Int. Ed.* **2008**, *47* (7), 1276–1279. https://doi.org/10.1002/anie.200703718.

(20) Giavarini, C.; Maccioni, F. Self-Preservation at Low Pressures of Methane Hydrates with Various Gas Contents. *Ind. Eng. Chem. Res.* **2004**, *43* (20), 6616–6621. https://doi.org/10.1021/ie040038a.

(21) Circone, S.; Stern, L. A.; Kirby, S. H. The Effect of Elevated Methane Pressure on Methane Hydrate Dissociation. *Am. Mineral.* **2004**, *89* (8–9), 1192–1201. https://doi.org/10.2138/am-2004-8-905.

(22) Falenty, A.; Kuhs, W. F.; Glockzin, M.; Rehder, G. "self-Preservation" of CH4 Hydrates for Gas Transport Technology: Pressure-Temperature Dependence and Ice Microstructures. *Energy and Fuels* **2014**, *28* (10), 6275–6283. https://doi.org/10.1021/ef501409g.

(23) Kida, M.; Watanabe, M.; Jin, Y.; Nagao, J. Pressurization Effects on Methane Hydrate Dissociation. *Jpn. J. Appl. Phys.* **2014**, *53* (1). https://doi.org/10.7567/JJAP.53.018003.

(24) Kida, M.; Jin, Y.; Watanabe, M.; Murayama, T.; Nagao, J. Improvement of Gas Hydrate Preservation by Increasing Compression Pressure to Simple Hydrates of Methane, Ethane, and Propane. *Jpn. J. Appl. Phys.* **2017**, *56* (9). https://doi.org/10.7567/JJAP.56.095601.

(25) Evgeny Chuvilin Olga Guryeva, B. B. Experimental Study of Self-Preservation Mechanisms during Gas Hydrate Decomposition In Frozen Sediments. *Proc. 7th Int. Conf. Gas Hydrates* **2011**, *7* (495), 92102.

(26) Falenty, A.; Kuhs, W. F. "Self-Preservation" of CO2 Gas Hydrates-Surface Microstructure and Ice Perfection. *J. Phys. Chem. B* **2009**, *113* (49), 15975–15988. https://doi.org/10.1021/jp906859a.

(27) Almenningen, S.; Flatlandsmo, J.; Fernø, M. A.; Ersland, G. Multiscale Laboratory Verification of Depressurization for Production of Sedimentary Methane Hydrates. *SPE J.* **2017**, *22* (01), 138–147. https://doi.org/10.2118/180015-PA.

(28) Tohidi, B.; Anderson, R.; Clennell, M. Ben; Burgass, R. W.; Biderkab, A. B. Visual Observation of Gas-Hydrate Formation and Dissociation in Synthetic Porous Media by Means of Glass Micromodels. *Geology* **2001**, *29* (9), 867–870. https://doi.org/10.1130/0091-7613(2001)029<0867:VOOGHF>2.0.CO;2.

(29) Katsuki, D.; Ohmura, R.; Ebinuma, T.; Narita, H. Visual Observation of Dissociation of Methane Hydrate Crystals in a Glass Micro Model: Production and Transfer of Methane. *J. Appl. Phys.* **2008**, *104* (8). https://doi.org/10.1063/1.3000622.

(30) Hauge, L. P.; Gauteplass, J.; Høyland, M. D.; Ersland, G.; Kovscek, A.; Fernø, M. A. Pore-Level Hydrate Formation Mechanisms Using Realistic Rock Structures in High-Pressure Silicon Micromodels. *Int. J. Greenh. Gas Control* **2016**, *53*, 178–186. https://doi.org/10.1016/j.ijggc.2016.06.017.

(31) Almenningen, S.; Flatlandsmo, J.; Kovscek, A. R.; Ersland, G.; Fernø, M. A. Determination of Pore-Scale Hydrate Phase Equilibria in Sediments Using Lab-on-a-Chip Technology. *Lab Chip* **2017**, *17* (23), 4070–4076. https://doi.org/10.1039/c7lc00719a.

(32) Almenningen, S.; Iden, E.; Fernø, M. A.; Ersland, G. Salinity Effects on Pore-Scale Methane Gas Hydrate Dissociation. *J. Geophys. Res. Solid Earth* **2018**, *123* (7), 5599–5608. https://doi.org/10.1029/2017JB015345.

(33) Almenningen, S.; Gauteplass, J.; Fotland, P.; Aastveit, G. L.; Barth, T.; Ersland, G. Visualization of Hydrate Formation during CO2 Storage in Water-Saturated Sandstone. *Int. J. Greenh. Gas Control* **2018**, *79* (November), 272–278. https://doi.org/10.1016/j.ijggc.2018.11.008.

(34) Chaouachi, M.; Falenty, A.; Sell, K.; Enzmann, F.; Kersten, M.; Haberthür, D.; Kuhs, W. F. In-Situ Micro-Structural Studies of Gas Hydrate Formation in Sedimentary Matrices. *EGU Gen. Assem. Conf. Abstr.* **2015**, *17*, 1–12. https://doi.org/10.1002/2015GC005811.Received.

(35) Sun, C. Y.; Peng, B. Z.; Dandekar, A.; Ma, Q. L.; Chen, G. J. Studies on Hydrate Film Growth. *Annu. Reports Sect. "C" (Physical Chem.* **2010**, *106*, 77. https://doi.org/10.1039/b811053k.

(36) Mochizuki, T.; Mori, Y. H. Clathrate-Hydrate Film Growth along Water/Hydrate-Former Phase Boundaries-Numerical Heat-Transfer Study. *J. Cryst. Growth* **2006**, *290* (2), 642–652. https://doi.org/10.1016/j.jcrysgro.2006.01.036.

(37) Peng, B. Z.; Dandekar, A.; Sun, C. Y.; Luo, H.; Ma, Q. L.; Pang, W. X.; Chen, G. J. Hydrate Film Growth on the Surface of a Gas Bubble Suspended in Water. *J. Phys. Chem. B* **2007**, *111* (43), 12485–12493. https://doi.org/10.1021/jp074606m.

(38) Katsuki, D.; Ohmura, R.; Ebinuma, T.; Narita, H. Methane Hydrate Crystal Growth in a Porous Medium Filled with Methane-Saturated Liquid Water. *Philos. Mag.* **2007**, *87* (7), 1057–1069. https://doi.org/10.1080/14786430601021652.

(39) Bylov, M.; Rasmussen, P. Experimental Determination of Refractive Index of Gas Hydrates. *Chem. Eng. Sci.* **1997**, *52* (19), 3295–3301. https://doi.org/10.1016/S0009-2509(97)00144-9.

(40) Kumar, A.; Maini, B.; P.R. Bishnoi; Clarke, M.; Zatsepina, O.; Srinivasan, S. Experimental Determination of Permeability in the Presence of Hydrates and Its Effect on the Dissociation

899 Characteristics of Gas Hydrates in Porous Media. *J. Pet. Sci. Eng.* **2010**, *70* (1–2), 114–122.
900 https://doi.org/10.1016/j.petrol.2009.10.005.

901 (41) Berge, L. I.; Jacobsen, K. A.; Solstad, A. Measured Acoustic Wave Velocities of R11
902 (CCl3F) Hydrate Samples with and without Sand as a Function of Hydrate Concentration.
903 *J. Geophys. Res. Solid Earth* **1999**, *104* (B7), 15415–15424.
904 https://doi.org/10.1029/1999jb900098.

905 (42) Ohmura, R.; Matsuda, S.; Uchida, T.; Ebinuma, T.; Narita, H. Clathrate Hydrate Crystal
906 Growth in Liquid Water Saturated with a Guest Substance: Observations in a Methane +
907 Water System. *Cryst. Growth Des.* **2005**, *5* (3), 953–957.
908 https://doi.org/10.1021/cg049675u.

909 (43) Servio, P.; Englezos, P. Morphology of Methane and Carbon Dioxide Hydrates Formed
910 from Water Droplets. **2003**, *49* (1), 269–276.

911 (44) Yan, C.; Li, Y.; Cheng, Y.; Wang, W.; Song, B.; Deng, F.; Feng, Y. Sand Production
912 Evaluation during Gas Production from Natural Gas Hydrates. *J. Nat. Gas Sci. Eng.* **2018**,
913 *57* (May), 77–88. https://doi.org/10.1016/j.jngse.2018.07.006.

914 (45) Zheng, R.; Li, S.; Li, X. Sensitivity Analysis of Hydrate Dissociation Front Conditioned to
915 Depressurization and Wellbore Heating. *Mar. Pet. Geol.* **2018**, *91* (December 2017), 631–
916 638. https://doi.org/10.1016/j.marpetgeo.2018.01.010.

917 (46) Behseresht, J.; Bryant, S. L. Sedimentological Control on Saturation Distribution in Arctic
918 Gas-Hydrate-Bearing Sands. *Earth Planet. Sci. Lett.* **2012**, *341–344*, 114–127.
919 https://doi.org/10.1016/j.epsl.2012.06.019.

(47) Riley, D.; Marin-Moreno, H.; Minshull, T. A. The Effect of Heterogeneities in Hydrate Saturation on Gas Production from Natural Systems. *J. Pet. Sci. Eng.* **2019**, *183* (June), 106452. https://doi.org/10.1016/j.petrol.2019.106452.

(48) Kneafsey, T. J.; Rees, E. V. L.; Nakagawa, S.; Kwon, T. Examination of Hydrate Formation Methods : Trying to Create Representative Samples Examination of Hydrate Formation Methods : Trying to Create Representative Samples. **2010**, 1–21.

(49) Vladimir Istomin Sergey Dolgaev, V. K. Metastability in Gas Hydrates Formation and Decomposition. *Proc. 7th Int. Conf. Gas Hydrates* **2011**, No. March.

(50) Chuvilin, E. M.; Istomin, V. A.; Safonov, S. S. Residual Nonclathrated Water in Sediments in Equilibrium with Gas Hydrate. Comparison with Unfrozen Water. *Cold Reg. Sci. Technol.* **2011**, *68* (1–2), 68–73. https://doi.org/10.1016/j.coldregions.2011.05.006.

(51) Istomin, V.; Chuvilin, E.; Bukhanov, B.; Uchida, T. Pore Water Content in Equilibrium with Ice or Gas Hydrate in Sediments. *Cold Reg. Sci. Technol.* **2017**, *137*, 60–67. https://doi.org/10.1016/j.coldregions.2017.02.005.

(52) Hashemi, S.; Macchi, A.; Bergeron, S.; Servio, P. Prediction of Methane and Carbon Dioxide Solubility in Water in the Presence of Hydrate. *Fluid Phase Equilib.* **2006**, *246* (1–2), 131–136. https://doi.org/10.1016/j.fluid.2006.05.010.

(53) Servio, P.; Englezos, P. Effect of Temperature and Pressure on the Solubility of Carbon Dioxide in Water in the Presence of Gas Hydrate. *Fluid Phase Equilib.* **2001**, *190* (1–2), 127–134. https://doi.org/10.1016/S0378-3812(01)00598-2.

(54) Chuvilin, E.; Davletshina, D. Formation and Accumulation of Pore Methane Hydrates in Permafrost: Experimental Modeling. *Geosci.* **2018**, *8* (12), 12–14. https://doi.org/10.3390/geosciences8120467.

(55) J. van Huissteden. *Thawing Permafrost-Permafrost Carbon in a Warming Arctic*; Springer Nature Switzerland AG 2020, 2020. https://doi.org/https://doi.org/10.1007/978-3-030-31379-1.

(56) Rivkina, E.; Gilichinsky, D. A.; McKay, C.; Dallimore, S. Methane Distribution in Permafrost: Evidence for an Interpore Pressure Methane Hydrate. In *Permafrost Response on Economic Development, Environmental Security and Natural Resources*; Paepe, R., Melnikov, V. P., Van Overloop, E., Gorokhov, V. D., Eds.; Springer Netherlands: Dordrecht, 2001; pp 487–496. https://doi.org/10.1007/978-94-010-0684-2_33.

(57) Hong, H.; Pooladi-Darvish, M.; Bishnoi, P. R. Analytical Modelling of Gas Production from Hydrates in Porous Media. *J. Can. Pet. Technol.* **2003**, *42* (11), 45–56. https://doi.org/10.2118/03-11-05.

(58) Davies, S. R.; Selim, M. S.; Sloan, E. D.; Bollavaram, P.; Peters, D. J. Hydrate Plug Dissociation. *AIChE J.* **2006**, *52* (12), 4016–4027. https://doi.org/10.1002/aic.11005.

(59) Tang, L. G.; Li, X. Sen; Feng, Z. P.; Li, G.; Fan, S. S. Control Mechanisms for Gas Hydrate Production by Depressurization in Different Scale Hydrate Reservoirs. *Energy and Fuels* **2007**, *21* (1), 227–233. https://doi.org/10.1021/ef0601869.

(60) Seol, Y.; Myshakin, E. Experimental and Numerical Observations of Hydrate Reformation during Depressurization in a Core-Scale Reactor. *Energy and Fuels* **2011**, *25* (3), 1099–

1110. https://doi.org/10.1021/ef1014567.

(61) Kneafsey, T. J.; Seol, Y.; Gupta, A.; Tomutsa, L. Permeability of Laboratory-Formed Methane-Hydrate-Bearing Sand: Measurements and Observations Using X-Ray Computed Tomography. *SPE J.* **2011**, *16* (1), 78–94. https://doi.org/10.2118/139525-PA.

(62) Singh, H.; Myshakin, E. M.; Seol, Y. A Nonempirical Relative Permeability Model for Hydrate-Bearing Sediments. *SPE J.* **2019**, *24* (2), 547–562. https://doi.org/10.2118/193996-PA.

(63) Makogon, Y. F.; Ghassemi, A. Effects of Self-Preservation of Natural Gas-Hydrates. *44th US Rock Mech. Symp. - 5th US/Canada Rock Mech. Symp.* **2010**.

(64) Park, J.; Shin, K.; Kim, J.; Lee, H.; Seo, Y.; Maeda, N.; Tian, W.; Wood, C. D. Effect of Hydrate Shell Formation on the Stability of Dry Water. *J. Phys. Chem. C* **2015**, *119* (4), 1690–1699. https://doi.org/10.1021/jp510603q.

(65) Bhade, P.; Phirani, J. Gas Production from Layered Methane Hydrate Reservoirs. *Energy* **2015**, *82*, 686–696. https://doi.org/10.1016/j.energy.2015.01.077.

(66) Holder, G. D.; Angert, P. F. Simulation of Gas Production from a Reservoir Containing Both Gas Hydrates and Free Natural Gas. *Proc. - SPE Annu. Tech. Conf. Exhib.* **1982**, *1982-Septe*. https://doi.org/10.2523/11105-ms.

(67) Chen, X.; Espinoza, D. N. Surface Area Controls Gas Hydrate Dissociation Kinetics in Porous Media. *Fuel* **2018**, *234* (July), 358–363. https://doi.org/10.1016/j.fuel.2018.07.030.

(68) Jarrar, Z. A.; Alshibli, K. A.; Al-Raoush, R. I.; Jung, J. 3D Measurements of Hydrate

Surface Area during Hydrate Dissociation in Porous Media Using Dynamic 3D Imaging. *Fuel* **2020**, *265* (October 2019), 116978. https://doi.org/10.1016/j.fuel.2019.116978.

(69) Takeya, S.; Shimada, W.; Kamata, Y.; Ebinuma, T.; Uchida, T.; Nagao, J.; Narita, H. In Situ X-Ray Diffraction Measurements of the Self-Preservation Effect of CH4 Hydrate. *J. Phys. Chem. A* **2001**, *105* (42), 9756–9759. https://doi.org/10.1021/jp011435r.

(70) Sun, C. Y.; Chen, G. J. Methane Hydrate Dissociation above 0 °c and below 0°C. *Fluid Phase Equilib.* **2006**, *242* (2), 123–128. https://doi.org/10.1016/j.fluid.2006.01.025.

(71) Chuvilin, E.; Davletshina, D.; Ekimova, V.; Bukhanov, B.; Shakhova, N.; Semiletov, I. Role of Warming in Destabilization of Intrapermafrost Gas Hydrates in the Arctic Shelf: Experimental Modeling. *Geosci.* **2019**, *9* (10), 1–12. https://doi.org/10.3390/geosciences9100407.

(72) Konno, Y.; Jin, Y.; Shinjou, K.; Nagao, J. Experimental Evaluation of the Gas Recovery Factor of Methane Hydrate in Sandy Sediment. *RSC Adv.* **2014**, *4* (93), 51666–51675. https://doi.org/10.1039/c4ra08822k.

(73) Melnikov, V. P.; Nesterov, A. N.; Reshetnikov, A. M.; Zavodovsky, A. G. Evidence of Liquid Water Formation during Methane Hydrates Dissociation below the Ice Point. *Chem. Eng. Sci.* **2009**, *64* (6), 1160–1166. https://doi.org/10.1016/j.ces.2008.10.067.

(74) KOMAI, T.; YAMAMOTO, Y.; OHGA, K. Dynamics of Reformation and Replacement of CO2 and CH4 Gas Hydrates. *Ann. N. Y. Acad. Sci.* **2006**, *912* (1), 272–280. https://doi.org/10.1111/j.1749-6632.2000.tb06781.x.

(75) Yamamoto, K.; Kanno, T.; Wang, X. X.; Tamaki, M.; Fujii, T.; Chee, S. S.; Wang, X. W.; Pimenov, V.; Shako, V. Thermal Responses of a Gas Hydrate-Bearing Sediment to a Depressurization Operation. *RSC Adv.* **2017**, *7* (10), 5554–5577. https://doi.org/10.1039/c6ra26487e.

(76) Yang, L.; Falenty, Andrzej , Chaouachi, M.; Haberthuer, David , Kuhs, Werner, F. Publications. *Geochemistry Geophys. Geosystems* **2016**, *17* (9), 1–16. https://doi.org/10.1002/2016GC006521.Received.

(77) Wang, B.; Dong, H.; Liu, Y. Y.; Lv, X.; Liu, Y. Y.; Zhao, J.; Song, Y. Evaluation of Thermal Stimulation on Gas Production from Depressurized Methane Hydrate Deposits☆. *Appl. Energy* **2018**, *227* (January 2017), 710–718. https://doi.org/10.1016/j.apenergy.2017.08.005.

(78) Song, Y.; Cheng, C.; Zhao, J.; Zhu, Z.; Liu, W.; Yang, M.; Xue, K. Evaluation of Gas Production from Methane Hydrates Using Depressurization, Thermal Stimulation and Combined Methods. *Appl. Energy* **2015**, *145*, 265–277. https://doi.org/10.1016/j.apenergy.2015.02.040.

(79) Ruppel, C. Methane Hydrates and the Future of Natural Gas. *MITEI Nat. gas Report, Suppl. Pap. Methane Hydrates 4* **2011**, 1–25.

(80) Chuvilin, E.; Lupachik, M.; Gory, L. Investigation of Gas Hydrate Formation in Frozen and Thawing Gas Saturated Sediments. *7th Int. Conf. Gas Hydrates* **2011**, No. Icgh.